

1 **Investigating the Frequency and **Inter-Annual Variability** in Global Above-Cloud Aerosol**
2 **Characteristics with CALIOP and OMI**

3
4

5 Ricardo Alfaro-Contreras¹, Jianglong Zhang¹, James R. Campbell² and Jeffrey S. Reid²

6
7

8 ¹Department of Atmospheric Science, University of North Dakota, Grand Forks, ND

9 ²Marine Meteorology Division, Naval Research Laboratory, Monterey, CA

10
11

12 Submitted to ACP

13 **July**

14 2015

15
16

17 _____

18 Corresponding Author Contact: Dr. Jianglong Zhang, c/o Department of Atmospheric Sciences,
19 4149 University Avenue Stop 9006, University of North Dakota, Grand Forks, ND, USA

20
21 E-mail: jzhang@atmos.und.edu

22

ABSTRACT

23
24 Seven and a half years (June 2006-November 2013) of Cloud-Aerosol Lidar with Orthogonal
25 Polarization (CALIOP) aerosol and cloud layer products are compared with collocated Ozone
26 Monitoring Instrument (OMI) Aerosol Index (AI) data and Aqua Moderate Resolution Imaging
27 Spectroradiometer (MODIS) cloud products, to investigate variability in estimates of bi-annual
28 and monthly above-cloud aerosol (ACA) events globally. The active- (CALIOP) and passive-
29 based (OMI-MODIS) techniques have their advantages and caveats for ACA detection, and thus
30 both are used to get a thorough and robust comparison of daytime cloudy-sky ACA distribution
31 and climatology. For the first time, baseline above cloud aerosol optical depth (ACAOD) and AI
32 thresholds are derived and examined ($AI = 1.0$, $ACAOD = 0.015$) for each sensor. Both OMI-
33 MODIS and CALIOP-based daytime spatial distributions of ACA events show similar patterns
34 during both study periods (December – May) and (June – November). Divergence exists in
35 some regions, however, such as Southeast Asia during June through November, where daytime
36 cloudy-sky ACA frequencies of up to 10% are found from CALIOP yet are non-existent from
37 the OMI-based method. Conversely, annual cloudy-sky ACA frequencies of 20-30% are reported
38 over Northern Africa from the OMI-based method, yet are largely undetected by the CALIOP-
39 based method. **Using a collocated OMI-MODIS-CALIOP dataset, our study suggests that the**
40 **cloudy-sky ACA frequency differences between the OMI-MODIS- and CALIOP-based methods**
41 **are mostly due to differences in cloud detection capability between MODIS and CALIOP as well**
42 **as QA flags used.** An increasing **inter-annual-variability of ~0.3-0.4%** per year (since 2009) in
43 global monthly cloudy-sky ACA daytime frequency of occurrence is found using the OMI-
44 MODIS based method. Yet, CALIOP-based global daytime ACA frequencies exhibit a near-
45 zero **inter-annual-variability**. Further analysis suggests that the OMI derived **inter-annual-**
46 **variability of** cloudy-sky ACA frequency may be affected by OMI row anomalies in later years.

47 A few regions are found to have increasing **slopes in inter-annual variability of** cloudy-sky ACA
48 frequency, including the Middle-East and India. Regions with slightly negative slopes of **the**
49 **inter-annual variability of** cloudy-sky ACA frequencies are found over South America and
50 **China**, while remaining regions in the study show nearly **zero change in ACA frequencies over**
51 **time. The inter-annual variability of ACA frequency are not statistically significant on both**
52 **global and regional scales**, though, given relatively lacking sample sizes. A longer data record of
53 ACA events is needed in order to establish significant trends of ACA frequency regionally and
54 globally.

55

56 **1. Introduction**

57 The above-cloud aerosol (ACA) phenomenon, wherein significant active-based
58 backscatter and passive-based scattered solar radiances are induced by particles above what are
59 predominately lower tropospheric clouds, has gained an increased amount of attention from the
60 scientific community (e.g. Haywood et al., 2004; Wilcox et al., 2009; Coddington et al., 2010;
61 Devasthale and Thomas, 2011; Wilcox, 2012; Kacenelenbogen et al, 2014). In particular,
62 whereas passive-based atmospheric retrievals are compromised by a binding inability to
63 decouple aerosol, cloud and atmospheric radiances in the ACA scenario, corresponding cloud
64 property retrievals are uniquely biased (Wilcox et al., 2009; Meyer et al., 2013; Alfaro-Contreras
65 et al., 2014; Li et al., 2014). ACA further perturbs regional radiation budgets by absorbing and
66 reflecting radiation from the cloud layers underneath the unidentified aerosol particle layer (e.g.,
67 Haywood et al., 2004), which again must be accounted for when estimating global cloud and
68 aerosol forcing budgets and regional semi-direct impact on static stability and cloud feedback.
69 Global oceans are covered with clouds nearly 70% of the time (e.g. Rossow and Schiffer, 1999),
70 with almost non-existent corresponding ground-based verification data of ACA phenomena.
71 This exacerbates the impact of ACA effects globally, limiting characterization of any
72 quantitative impact and frequency of occurrence almost exclusively to satellite-based
73 measurements.

74 ACA events are most effectively identified using active-based lidar measurements, which
75 has been demonstrated using the Cloud-Aerosol Lidar with Orthogonal Polarization (CALIOP;
76 Winker et al., 2010; Kacenelenbogen et al, 2014), the lone such instrument presently in satellite
77 orbit. CALIOP measures backscattered signals at the 532 and 1064 nm wavelengths, including
78 segregated linearly-parallel and orthogonal polarization backscatter states in the former channel.

79 In particular, the active-profiling element is essential for decoupling aerosol and cloud scattering
80 contributions in ACA events (Devasthale and Thomas, 2011). Utilizing four years of CALIOP
81 Level 2 data (Winker et al., 2009), Devasthale and Thomas (2011) evaluated seasonal and
82 latitudinal patterns of ACA for liquid water cloud events. Alfaro-Contreras et al. (2014) describe
83 seasonal frequencies in ACA over the southern Atlantic Ocean off the West African coastline as
84 well as over the Gulf of Tonkin in Southeast Asia where high ACA loading episodes were found
85 during the summer and fall months and early spring months, respectively.

86 Whereas limited process studies have helped raise awareness of the ACA problem
87 overall, **year to year variability** in global ACA frequency distribution has not yet been developed
88 with CALIOP. Despite a nearly eight-year (2006-present) CALIOP data archive available, one
89 must be considerate of the fact that satellite lidar profiling is constrained presently to a single
90 laser-illuminated curtain and roughly sixteen daily orbits of the planet. Questions thus arise about
91 the representativeness of CALIOP datasets for some climatological analyses, like ACA, given its
92 temporal persistence and spatial extent (Devasthale and Thomas, 2011; Yu et al., 2012).
93 Additionally, for CALIPSO-based ACA studies to be meaningful, the potential impacts of signal
94 deterioration to CALIOP derived aerosol optical depth (AOD) values need to be known. Despite
95 the practical limitations of applying passive sensors for studying phenomena like ACA, then, the
96 relatively wide field-of-view on passive imagers renders far greater data volume, which makes
97 them more ideal options for a long-term study.

98 Ozone Monitoring Instrument (OMI) measurements have also been used for studying
99 ACA events (e.g., Wilcox et al., 2009; Yu et al., 2012; Alfaro-Contreras et al., 2014). In
100 particular, the OMI Aerosol Index (AI), computed using the difference between observed and
101 calculated ultraviolet (UV) radiances (Torres et al., 2007), has been used to locate UV-absorbing

102 aerosols suspended over bright cloud decks (e.g. Yu et al., 2012, Torres et al., 2012). This
103 technique, originally used on the Total Ozone Mapping Spectrometer (TOMS), can only be used
104 to detect UV-absorbing aerosols, such as biomass burning smoke and desert dust aerosols and is
105 sensitive to underneath cloud properties (e.g. Yu et al., 2012; Alfaro-Contreras et al., 2014).
106 Further and compared with CALIOP, OMI measurements represent a relatively large surface
107 footprint of 13x24 km at nadir, which limits cloud-clearing efficacies since footprints of this size
108 are prone to sub-pixel cloud contamination (Torres et al., 2007). Collocated Moderate Resolution
109 Imaging Spectroradiometer (MODIS) observations, however, as part of NASA's A-Train
110 satellite constellation, which includes CALIOP (Stephens et al., 2002), can be utilized to
111 distinguish and filter cloudy pixels/scenes within the OMI footprint.

112 Comparison of active vs. passive based sensors for evaluating the spatio-temporal
113 coverage of ACA events, and for studying **inter-annual variability** of ACA occurrence **on**
114 **regional and global scales**, represents a conservative means for conceptualizing the breadth of the
115 problem. The goal of this work is, therefore, to compare and contrast distributions in global and
116 regional ACA frequencies and their **year-to-year variability** using both CALIOP- and OMI-
117 based approaches. Caveats to each approach are specifically identified, and thus qualified within
118 the discussion so as to keep comparison as consistent and robust as possible. We highlight
119 regions particularly susceptible to ACA occurrence, establishing a baseline for future ACA-
120 induced biases in satellite cloud property retrievals overall.

121

122 **2. Datasets and Methodology**

123 CALIOP Level 2 5-km cloud and aerosol layer products (Winker et al., 2010) and OMI
124 Level 2 Collection 3 UV aerosol products (OMAERUV; Torres et al., 2007) are paired with
125 Aqua MODIS cloud products (MYD06_L2; King et al., 1997) and Aerosol Robotic Network

126 (AERONET; Holben et al., 1998) Level 2.0 Version 2 cloud-screened data from June 2006
127 through November 2013.

128 For identification of ACA, 5-km CALIOP 532 nm cloud and aerosol layer products are
129 used (Winker et al., 2009, 2010) for resolving aerosol extinction above apparent cloud top
130 heights in each respective product file (e.g. Yu et al., 2012; Alfaro-Contreras et al., 2014). The
131 532 nm above cloud aerosol optical depth (ACAOD) is then solved by integrating the extinction
132 coefficient over those corresponding bins (Liu et al., 2013; Kacenelebogen et al., 2014). The
133 CALIOP-based **inter-annual variability** analysis may be affected by CALIOP signal deterioration
134 over time. Thus, collocated AERONET datasets are used, as first order approximation, for
135 evaluating instrument-related **variation in the year-to-year variability** of CALIOP AOD.
136 Reported at eight spectral bands ranging from 0.34 μm – 1.64 μm (Holben et al., 1998),
137 AERONET AOD datasets are frequently used for validating satellite retrievals (e.g., Zhang et al.,
138 2001; Yu et al., 2003; Kaufman et al. 2005; Remer et al., 2005; Hahn et al., 2010; Shi et al. 2011;
139 Sayer et al. 2012), as well as model simulated aerosol optical properties (e.g. Zhang et al., 2011;
140 2014).

141 The Level 2.0 cloud-screened and quality-assured AERONET AOD data (Eck et al.,
142 1999) from all available coastal and island AERONET sites are used for collocating CALIOP
143 data. AERONET AOD data are interpolated, based on a method described in Zhang and Reid
144 (2006), to the 0.532 μm **CALIOP wavelength** and are spatio-temporally-located with
145 CALIOP AOD data. **Year-to-year changes in the AOD retrieved from the CALIOP instrument**
146 are investigated by calculating the global monthly-mean AERONET and CALIOP AODs and
147 comparing the two monthly aerosol loading averages. CALIOP observations found to be within
148 0.3 degrees latitude/longitude and ± 30 minutes of corresponding AERONET observations are

149 considered collocated in space and time. In addition, we have used only pairs that have
150 collocated AERONET AOD ($0.532 \mu\text{m}$) data less than 0.2 to exclude major aerosol episodes of
151 continental origin. One additional quality assurance step is applied to exclude pairs with
152 CALIOP AOD of larger than 0.6 for removing potentially noisy CALIOP data. In the case where
153 several CALIOP observations are paired up with a single AERONET retrieval, a one-to-one
154 relationship is established with the closest CALIOP observation.

155 OMI AI are used to isolate ACA events in those data. OMI AI and MODIS cloud
156 datasets are spatio-temporally-collocated, given their position in the NASA “A-Train”
157 constellation (e.g. Stephens et al., 2002), by collocating the two products with respect to
158 overpass times and then identifying all temporally-collocated cloudy MODIS pixels located
159 within the boundaries of the OMI footprint. Such methods are described further in Alfaro-
160 Contreras et al. (2014). Cloud fractions from the MODIS MYD06 product, reported at a 5 km
161 horizontal resolution, are then leveraged for sub-pixel cloud clearing of the OMI AI. The
162 MODIS cloud fraction is computed from the percentage of cloudy 1-km cloud mask product
163 (MOD35) pixels within a given 5-km scene (e.g., Ackerman et al., 1998). The, OMI and
164 MODIS data are each filtered and quality-assured (described in detail in Alfaro-Contreras et al.,
165 2014) to calculate respective global ACA distributions. **The OMI and MODIS data are spatially
166 and temporally collocated, and the collocated OMI AIs are assigned to 100% cloudy MODIS
167 scenes (as determined by MODIS, with a COD > 0). This collocation process and methods are
168 further described in Alfaro-Contreras et al. (2014). However, cloud inhomogeneity is not
169 considered, and we leave the topic for another study.**

170 **If multi-layer clouds exist, MODIS can only resolve the highest cloud layer most of the**
171 **time. Thus, we focus on the highest level clouds in any given atmospheric column using**

172 CALIOP cloud layer products for a more accurate representation between the two techniques.
173 The CALIOP data are filtered based on the study by Yu et al. (2012), where aerosol layers found
174 with ‘medium’ or ‘high’ confidence are used. Note that, initially, cloudy scenes are defined as
175 CALIOP COD > 0 for the CALIOP-based method and no QA steps are applied to the CALIOP
176 cloud layer products to ensure the detection of all possible ACA events. The effect of QA flags
177 of the CALIOP cloud layer products to the detected CALIOP ACA frequency is further explored
178 in Section 4.2 (as well as shown in Devasthale and Thomas, 2011). It is known that that the
179 OMI instrument has experienced row anomalies since 2008-2009
180 (<http://www.knmi.nl/omi/research/product/>, accessed on 22 Dec. 2014). Thus, the impact of the
181 row anomalies on the inter-annual variability of ACA occurrence derived from OMI AI is
182 explored later in this paper.

183

184 **3. Above-Cloud Aerosol Baselines and Limitations**

185 There are always aerosol particles above clouds (a fact that quickly becomes lost when
186 discussing the basic physics of ACA relative to satellite observation). Therefore, there exists
187 some baseline thresholds by which active backscatter and/or passive radiances become
188 significant relative to a given physical process or retrieval (i.e., radiative forcing, heating rates,
189 transmission estimates, cloud microphysical retrievals, etc.). Accordingly, each of the
190 instruments subject to the ACA phenomenon in this study exhibit fundamental sensitivities to
191 ACA detection, which impact our ability to characterize the problem fully. Therefore, the
192 baseline thresholds for significant ACA events need to be identified for both OMI- and CALIOP-
193 based ACA studies.

194 To conceptualize the problem, we look at the globally averaged cloud-top height for
195 clouds located under aerosol plumes, which is found to be roughly 2.0 km and compares well

196 with previous studies (Devasthale and Thomas, 2011). Thus, we consider the unique AERONET
197 site at Mauna Loa, Hawaii (LAT/LON, 3397 m above mean sea level). This free-tropospheric
198 ground site rests at an altitude roughly within the global mean cloud top heights. Indeed, this
199 physical feature of the site (that is being above the cloud deck below) is one of the key reasons
200 for the importance of the site globally. The yearly mean Level 2.0 AERONET AOD (500 nm)
201 there ranges from 0.013-0.023 (500 nm) from 1996-2013, and provides a generalized estimate
202 for potential baseline ACAOD value globally. Kacenelenbogen et al. (2014) report that the
203 CALIOP lidar exhibits limitations in detecting ACA plumes with ACAOD less than 0.02. This
204 lower value may, therefore, represent an effective noise floor, whereby CALIOP algorithm
205 response below it is compromised.

206 Based on Kacenelenbogen et al. (2014) as well as the AOD climatology from the Mauna
207 Loa AERONET site analyses, we arbitrarily set the baseline CALIOP ACAOD value to 0.015.
208 Still, the CALIOP ACAOD baseline of 0.015 is rather arbitrary, and thus, we investigate the
209 CALIOP-based ACA frequency distributions by varying the baseline values to 0, 0.01, 0.015 and
210 0.02 as shown in Fig. 1. Figures 1a-d show the cloudy-sky global ACA frequency distribution
211 from CALIOP, defined in Table 1, for the Dec.- May period, for baseline ACAODs of 0 (1a),
212 0.01 (1b), 0.015 (1c) and 0.02 (1d) respectively, using the CALIOP aerosol layer datasets. Note
213 that different from the cloudy-sky frequency, another way of measuring ACA frequency has
214 been proposed by Devasthale and Thomas (2011) and is referred as the all-sky frequency from
215 CALIOP in this study, also defined in Table 1. The difference between the two techniques is
216 discussed in more detail during the section analyzing the year to year variation in ACA
217 frequency occurrence.

218 Shown in Fig. 1, no clear difference is observed in the cloudy-sky ACA frequency by
219 applying various CALIOP ACAOD baselines. A similar conclusion can also be made for the
220 June- Nov period (Figs. 1e-1h). Thus, for the purposes of this paper, the baseline CALIOP
221 ACAOD value of 0.015 (0.532 μm) is chosen, and the sensitivity of ACA inter-annual variability
222 to the selection of the baseline CALIOP ACAOD is explored in a later section. Additionally, our
223 selection of CALIOP ACAOD baseline has little effect on the background cloudy-sky ACA
224 frequency, which is for the most part less than 5 % (dark blue) globally. Thus, we arbitrarily
225 select 5% as the threshold between background and significant cloudy-sky ACA frequencies. For
226 the remainder of the paper, ACA frequencies less than five percent are not considered for global
227 distributions of ACA frequencies (except for sensitivity and case studies).

228 To derive the corresponding noise floor value for above-cloud OMI AI, a pairwise
229 comparison of collocated above-cloud OMI AI and CALIOP AOD has been performed using
230 one year (2007) of collocated OMI-MODIS and CALIOP data, as described in Alfaro-Contreras
231 et al. (2014), though without any limitations on the cloud-top height. Figure 2a depicts the
232 relationship between binned above-cloud OMI AI and CALIOP AOD segregated into six
233 different underlying MODIS-derived CODs (Yu et al., 2012, Torres et al., 2012). The bin-
234 averaged CALIOP ACAOD of 0.015, the baseline CALIOP ACAOD value chosen above,
235 corresponds to OMI AI values of 0.7 - 1.2 for underlying MODIS CODs ranging from 0 to 20.
236 Note that, if CALIOP ACAODs are biased low, the corresponding OMI AI thresholds may bias
237 high using methods as shown in Fig. 2a.

238 Still, as suggested from Fig. 2a, baseline values of OMI AI vary from 0.7 to 1.2
239 depending on the underlying cloud properties. To further explore the issue, detected ACA events
240 are evaluated using different baseline OMI AI values, similar to the CALIOP ACAOD baseline

241 analysis and shown in Figs. 2b-2i, though using only those bin averages with cloudy-sky ACA
242 frequency greater than five percent. Figures 2b-2e depict the multi-year (2006-2013) cloudy-sky
243 ACA frequency global average for the Dec.-May period, by applying AI baseline thresholds of
244 0.7 (2b), 0.8 (2c), 0.9 (2d) and 1.0 (2e) respectively. With the use of the baseline OMI AI value
245 of 0.7, most of the remote southern oceans stand out for significant case numbers. By increasing
246 the AI baseline value to 1.0, in contrast, detected ACA events are significantly reduced. A
247 similar conclusion can also be drawn from the June-Nov. period (Figs. 2f-i). Given that hand-
248 held ship borne sun photometer measurements collected by the Marine Aerosol Network (MAN;
249 Smirnov et al., 2011) show an averaged AOD (0.55 μm) of 0.07 or less from 30° to 60° S (Toth
250 et al., 2013), significant ACA events are not likely over remote southern oceans. Thus, based on
251 Figs. 1 and 2, CALIOP ACAOD of 0.015 and an above-cloud OMI AI of 1.0 are chosen as
252 baselines. As we have now defined our baseline thresholds for ACA from both OMI and
253 CALIOP, this enables us to create definitions of the various ACA frequencies used throughout
254 this study, which are shown with further detail in Table. 1.

255 Selection of baseline CALIOP ACAOD and OMI AI is clearly subjective, and done for
256 qualitative analysis in subsequent sections. There are multiple caveats that must be considered
257 before constraining these values more accurately and representatively. First, as mentioned
258 earlier, the CALIOP instrument has issues in detecting distinct optically-thin aerosol layers,
259 especially during daytime. Additionally, it has been reported that CALIOP has a decreased
260 sensitivity to stratospheric aerosols layers (Thomason et al., 2007; Winker et al., 2009). Third,
261 besides aerosol loading, OMI AI is also sensitive to parameters such as aerosol vertical
262 distributions, cloud optical depth of underlying cloud and aerosol single scattering albedo (e.g.
263 Yu et al., 2012). Thus, setting a seasonal and regional based baseline for ACA requires a more in

264 depth analysis and should be considered in future studies. Still, this study presents the first ever
265 attempt to solve ACA baselines, and the thresholds selected are the best noise floors we can
266 **derive with the given inputs.**

267

268 **4. Comparison of ACA Global Climatology using Two Separate Techniques**

269 **4.1 ACA Global Climatology from all available MODIS, OMI and CALIOP data**

270 Figure 3a depicts the multi-year gridded mean near-global distribution (180°W - 180°E,
271 45°S - 60°N) of the OMI-derived daytime cloudy-sky ACA frequency (**defined in Table 1.**) for
272 December to May. Figures 3b and 3c show corresponding cloudy-sky daytime and nighttime
273 frequencies, respectively, using CALIOP data (**defined in Table.1**). Figures 3d-3f show the
274 corresponding information to Figs. 3a-3c for June to November.

275 Comparison of daytime cloudy-sky ACA frequency distributions is consistent between
276 the two sensors and seasonal periods investigated, and depicted in Figs. 3g-3j. Some differences
277 are distinct during December-May, as cloudy-sky ACA frequencies as high as 10 % are visible
278 over the Gulf of Mexico from CALIOP, for instance, whereas they are non-existent from OMI-
279 MODIS (**Fig. 3a**). Cloudy-sky ACA frequencies of 20-30 % are found with OMI-MODIS over
280 high-latitude northern Asia, in contrast with CALIOP that shows no such activity (**Fig. 3i**).
281 During June-November, both methods resolve ACA events over the west coast of Africa, as well
282 as over the Middle East, of similar magnitude (10-60%). However, distinct differences can be
283 found between the two datasets. Higher cloudy-sky ACA frequency values of 10-30% are found
284 over North Africa using OMI-MODIS, in contrast to much lower values of 10-20% found using
285 CALIOP, for example. An OMI-based ACA study should correspond with a higher noise floor
286 compared with that of an active sensor, based on OMI's much coarser spatial and vertical
287 resolutions, an inability to resolve non-UV absorbing aerosols, and the fundamental decoupling

288 of column-integrated radiances themselves. Still, if the OMI AI baseline is biased, it may
289 introduce an additional difference between OMI-MODIS- and CALIOP-based ACA frequencies.

290 Cloudy-sky ACA frequencies as high as 10-30 % are found over North Africa for both
291 periods from OMI-MODIS while CALIOP returns much lower percentages (10-20%) over the
292 same region. This region is dominated by dust particle transport (Kaufman et al. 2005), which is
293 detected by both OMI and CALIOP. Therefore, we suspect that their relative differences as
294 derived in Figs. 3i and 3j are likely linked to the misidentification of thick dust plumes as clouds
295 by the MODIS cloud-masking scheme over the bright desert surfaces (e.g., Levy et al., 2013).
296 Further differences observed between the two datasets may also be due to the different
297 algorithmic sensitivities exhibited to both the optical depth of the underlying cloud and overlying
298 aerosol plume, the OMI AI and CALIOP AOD noise floors used to define the ACA events, **the**
299 **particular QA settings applied to any of our data sets, difference in cloud-detection techniques**
300 **between CALIOP and MODIS or OMI's inability to detect all aerosol types. We have further**
301 **explored this issue in section 4.2.**

302 Compared with daytime, increases in both the spatial extent and cloudy-sky CALIOP
303 ACA frequencies are observable at night, as seen from Figs. 3b, c, e and f, over most regions.
304 Over the most common ACA regions, nighttime cloudy-sky ACA frequencies can be 10-30 %
305 higher than during day, which may partially due to the stronger sensitivity of CALIOP at night
306 allowing for detection of optically thin aerosol plumes. In particular, ACA events are observed
307 with extended frequency over the west coast of North America year round and over the west
308 coast of South America for the June-Nov. period. Cloudy-sky ACA frequencies at night, over
309 both of these regions, are composed of optically-thin aerosol loading cases above our defined
310 noise floor. Nighttime ACA events are also observed over the east coast of Asia year round.

311 One reason for differences in spatial coverage between daytime and nighttime ACA events is
312 plausibly linked to a lower planetary boundary layer that affects the formation of low clouds (e.g.
313 Schrage et al., 2012). Still, the discrepancy between nighttime and daytime ACA events can be
314 partially attributed to the potential detection of relatively optically thin above-cloud aerosol
315 plumes that are more detectable during nighttime compared with day as a result of the higher
316 signal to noise ratio for CALIOP nighttime data (e.g. Kacenelenbogen et al., 2014).

317 Shown in Fig. 4 are averaged above-cloud OMI AI and CALIOP AOD values for
318 corresponding ACA events from Fig. 3. Figure 4a depicts the mean near-global distribution of
319 OMI AI over MODIS-resolved cloudy skies, defined as OMI-MODIS collocated cloudy pixels
320 (cloud fraction of unity) and OMI AI averaged for each $1^\circ \times 1^\circ$ grid box, during December to
321 May. Only bins with averaged AI greater than 1.0 are plotted in accordance with our defined
322 noise floor. Figure 4b depicts multi-year mean gridded daytime CALIOP ACAOD averaged for
323 each $2.5^\circ \times 2.5^\circ$ grid box for CALIOP-defined cloudy pixels ($COD > 0$), using only bin averaged
324 ACAOD greater than 0.015, also for December-May. Figure 4c shows the same information as
325 Fig. 4b, now for nighttime CALIOP retrievals.

326 During the Dec.-May period, elevated OMI AI values are observed over the Saharan
327 desert region of northern Africa, as well as in Southeast Asia off the coast of northern Vietnam.
328 In comparison with OMI AI, CALIOP AOD shows a much broader distribution of AODs greater
329 than the baseline ($ACAOD > 0.015$) for the entire globe. Bin averaged AIs greater than the
330 baseline ($AI > 1.0$) are sparse during the winter and spring months. Additionally, optically thin
331 aerosol plumes are observed over the Northern Pacific Ocean during the CALIOP nighttime
332 analysis (Fig. 4c), when compared to the daytime (Fig. 4b), due to the absence of solar light
333 causing a decrease in sensitivity to the CALIOP lidar.

334 Figures 4d-4f depict the same information as Figs. 4a-4c, now for the Jun.-Nov. period.
335 This period exhibits a relatively large overall distribution of ACA events. In addition to the
336 Saharan dust outbreaks, elevated AI and AOD values over the southern Africa smoke region are
337 also found from both OMI and CALIOP datasets, respectively. This period exhibits large
338 aerosol loading and ACA frequency over Southern Africa and the southeast Atlantic Ocean.
339 High values of ACAOD are also found over the Indian Ocean and Arabian Sea, due likely to the
340 transport of dust aerosols from the east Saharan and Arabian Gulf regions (Satheesh et al., 2006).
341 Comparing Figs. 3 and 4 over regions such as the west coast of South and North America, it is
342 clear that cloudy-sky ACA frequencies are mostly attributable to relatively low aerosol loading
343 events. Figure 4 shows a drastically reduced distribution of averaged OMI AIs above the AI
344 baseline (1.0) in comparison to averaged CALIOP ACAODs above the AOD baseline (0.015).

345 Again, differences are visible here between day and nighttime CALIOP AOD
346 distributions. Off the Southwest coast of Africa, the development of marine stratus-type clouds,
347 as suggested from Fig. 4, may lead to higher ACAOD values at night. Over India and the
348 Middle East, we suspect that higher daytime ACAOD values may exist. Still, lower CALIOP
349 signal-to-noise during daytime may be a limiting factor that contributes significantly to the
350 difference.

351 It is likely that most ACA events occur over low-level liquid-phase cloud decks.
352 Therefore, spatial distributions of CALIOP-derived low-level clouds are investigated. Figure 5a
353 (5b) depicts the daytime (nighttime) multi-year mean distribution of low-level clouds (defined as
354 the ratio of CALIOP scenes with a COD > 0 and cloud-top height < 3km over total number of
355 CALIOP scenes) during December 2006 – May 2013. CALIOP cloud layer data are gridded into
356 2.5° x 2.5° bins. Figures 5c and 5d depict the same information as Figs. 5a and 5b, now from

357 June 2006 – Nov. 2013. Figures 5e and 5f depict the ratio between daytime and nighttime low-
358 level cloud frequencies per bin for the Dec.-May period and June-Nov. periods, respectively. The
359 ratio is as high as 2.0 over the Northern and Southern Africa regions during June-Nov., as well as
360 over the Western US annually. Such a high ratio between day and nighttime data leads to a
361 nighttime frequency of 10-20 % low-level cloud coverage increase over most regions compared
362 with daytime observations, plausibly due to diurnal boundary layer effects.

363 A significant percentage of CALIOP-derived low-level clouds are plausibly
364 stratocumulus clouds, which are frequently observed over the west coasts of major continents
365 (e.g. Wood et al., 2012). Qualitative comparison of Figs. 4 and 5 indicates reasonable
366 consistency between high frequencies of CALIOP-defined low-level cloud formation and ACA
367 loading. With the exception of the Saharan region, again due to the possible misclassification of
368 thick aerosol plumes as clouds by MODIS discussed earlier, most ACA loading cases are found
369 where the CALIOP-defined low-level cloud formation six month frequency exceeds 20 % or
370 more. This indirectly confirms that most ACA outbreaks occur over CALIOP-defined low-level
371 clouds.

372 It is also useful to evaluate ACA frequency relative to mean clear-sky AOD. Figures 6a-6d
373 depict the multi-year mean clear-sky CALIOP AOD for the same temporal and spatial domains
374 as Figs 4b, c, e and f, respectively. As opposed to the cloud-sky ACA aerosol loading (Fig. 4),
375 AOD loading over clear-skies shows more activity inland, as the formation of low-level clouds is
376 more common over coastal regions (ICCP, 2007). An inter-comparison among Figs. 4, 5 and 6
377 suggests that ACA events do not necessarily follow clear sky AOD patterns but rather those
378 above-cloud aerosol-polluted regions with a high frequency of low-cloud presence.

379

380 **4.2 ACA Global Climatology from the collocated MODIS, OMI and CALIOP dataset**

381 As illustrated in Fig. 3 for the Dec.-May daytime period, ACA events over North Africa
382 as derived from the OMI-MODIS-based method are not found from the CALIOP-based method.
383 Also, ACA events over India, as reported from the CALIOP-based method, are not visible from
384 the OMI-MODIS-based method. Similarly, for the June-Nov. period, ACA events over North
385 Africa reported from the CALIOP-based method are not as frequent as those seen from the OMI-
386 MODIS-based method. Yet the ACA events detected from the CALIOP-based method over
387 Southern China are not visible from the OMI-MODIS-based method.

388 To unveil the differences between the OMI-MODIS- and CALIOP-based cloudy-sky
389 ACA global climatology, a collocated dataset has been constructed that includes spatially and
390 temporally-collocated MODIS, OMI and CALIOP data for the period of June 2006 – November
391 2008. Note that no collocated data are available after Nov. 2008 due to the row anomaly of the
392 OMI instrument. All three sensors are on board the A-train constellation, making temporal
393 collocation less of an issue, and we require the observational times of the three datasets to be
394 within +/- 30 minutes to be considered. To spatially collocate the three datasets, only MODIS
395 (OMI) observations that are within 0.04 degrees (0.2 degrees) of the center of a CALIOP data
396 point (from the 5-km CALIOP aerosol and cloud layer products) are used. Using the collocated
397 OMI-MODIS-CALIOP data set, the differences in cloudy-sky OMI-MODIS- and CALIOP-
398 based ACA frequencies are studied as functions of CALIOP cloud and aerosol QA flags
399 (Devastahale and Thomas, 2011), the differences between MODIS and CALIOP reported cloud
400 coverages, and aerosol properties (UV-absorbing versus non UV-absorbing aerosols).

401 Similar to Figs. 3b and 3a, Figs. 7a and 7d show the cloudy-sky ACA frequency as
402 detected by the CALIOP- and OMI-MODIS-based methods respectively, but with use the OMI-

403 MODIS-CALIOP collocated dataset, for the Dec.-May period. Figures 7b (7e) and 7c (7f) show
404 the all-sky ACA frequency and cloudy sky frequency for the CALIOP- (OMI-MODIS-) based
405 methods. As mentioned in Table 1, all-sky ACA frequency is defined as the number of ACA
406 events divided by all data points. Thus, Fig.s 7b (7e) and 7c (7f) can also be considered as ACA
407 event data counts and cloudy-sky data counts for the CALIOP- (OMI-MODIS-) based method.

408 The first thing to notice from these data is that cloudy sky frequency from the CALIOP-
409 based method is higher than that of the OMI-MODIS-based method. The differences in cloudy
410 sky frequencies are not unexpected, as the CALIOP-based method can detect optically-thin
411 clouds (such as thin cirrus clouds) that the OMI-MODIS-based method is limited (e.g., Toth et
412 al., 2013). Also, the all-sky ACA frequencies from CALIOP- and OMI-MODIS-based methods
413 show similar magnitudes for both the Dec.-May and June-Nov. periods. Thus, the higher cloud-
414 sky ACA events over North Africa, as reported from the OMI-MODIS-based methods, are likely
415 due to the differences in cloud detection capability among the different sensors.

416 For the Dec.-May period, higher all-sky ACA frequency is reported from the CALIOP-
417 based method over India. A similar situation is also found for the June-Nov. period over
418 Southeast Asia. While one would suspect that the higher ACA events over India and Southeast
419 Asia regions could be due to the fact that OMI-MODIS based method is only sensitive to non
420 UV-absorbing aerosols, we also evaluated the issue with respect to the CALIOP QA flags. Figure
421 8 shows the global plots of cloudy-sky ACA frequencies from the original QA metrics used to
422 generate Fig. 3, as well as global plots altering CALIOP aerosol and cloud QA flags to 'lenient',
423 'intermediate' and 'strict'. Here, the CAD scores and Feature Classification Flags are used to
424 define the quality of each retrieval. In order for a feature to be considered lenient, intermediate
425 or stringent quality, its CAD score absolute value must be greater than either 0, 20 and 70,

426 respectively. In addition, the feature flag must also return at least ‘low’, ‘medium’ and
427 ‘confident’ result for the ‘lenient’, ‘intermediate’ and ‘stringent’ QA levels, respectively as
428 defined in Liu et al. (2009).

429 Figures 8a-8c show the distributions of cloud fraction with the use of lenient,
430 intermediate and strict CALIOP cloud QAs, respectively. These data reflect how cloud QA
431 exhibits only a minor effect on the spatial distribution of cloud fraction. Figures 8d-8f show the
432 spatial distribution of cloudy-sky ACA frequency with the ‘lenient’ aerosol QA setting but with
433 the cloud QA levels of ‘lenient’, ‘intermediate’ and ‘strict’, respectively. Clearly seen from Figs.
434 8d and 8e, with the changing of cloud QA setting from ‘lenient’ to ‘intermediate’, are that the
435 CALIOP-based cloudy-sky ACA frequencies are much reduced over North Africa, the Middle-
436 East, India and Southern China. This indicates that a portion of the observed differences
437 between the OMI-MODIS- and CALIOP-based methods may due to cloud QA. Similarly, when
438 we hold the cloud QA setting constant at ‘lenient’ while varying the aerosol QA setting from
439 ‘lenient’ to ‘intermediate’ and ‘strict’ (Figs. 8g-8i), no significant changes in cloudy-sky ACA
440 frequencies are found. We repeat the process for the June-Nov. period, as shown in Figs. 8j-8r,
441 and similar conclusions are found.

442 The CALIPSO Level 2 cloud and aerosol layer products include cloud retrievals
443 conducted using horizontal averages at the three extended settings (e.g. 5, 20 or 80 km averages).
444 While 5 km averaging detects the most “reliable” cloud and aerosol signals, the 80-km averaging
445 locates features with “weaker” signals (Vaughan et al., 2009). Since the CALIPSO Level 2
446 cloud and aerosol layer products are used in this study, and thus, the results presented here shall
447 include horizontal averages from the three setting as mentioned. In addition, using CALIOP’s
448 ability to distinguish different aerosol types, we find that absorbing aerosols (dust, smoke and

449 polluted dust) constitute about 80 % of ACA particles over southeast Asia during June – Nov.,
450 and more than 90 % over India during the Dec. – May period. Thus, we do not expect OMI’s
451 inability to detect all aerosol types as a major cause for the observed ACA frequency differences
452 over these regions. On the contrary, the differences in cloud detection capability, the QA
453 settings and their arbitrary thresholds used are instead likelier be the primary causes for the
454 discrepancies between OMI-MODIS- and CALIOP-based methods. Still, aerosol type
455 discrimination from CALIOP measurements has its own limitations, and we leave this topic for a
456 future paper to explore.

457

458 **5. Inter-Annual Variability of Global ACA Frequency**

459 An analysis of the year-to-year variation in the global cloud-sky ACA frequency is
460 carried out for five different scenarios. The different scenarios are: OMI daytime cloudy-sky
461 frequency, CALIOP daytime cloudy-sky and all-sky frequencies and CALIOP nighttime cloudy-
462 sky and all-sky frequencies. As suggested from Section 4.2, only CALIOP data with both cloud
463 and aerosol QA settings as either ‘medium’ or ‘highest’ confidence levels are used hereafter.
464 Figure 9 shows CALIOP daytime cloudy-sky frequency (red) and all-sky frequency (blue),
465 CALIOP nighttime cloudy-sky frequency (orange) and all-sky frequency (purple), and OMI
466 daytime cloudy sky-frequency (green). Each data point represents the global monthly-mean
467 ACA frequency of CALIOP and OMI calculated from 2.5° and 1° gridded ACA frequencies,
468 respectively.

469 An increase in the OMI cloudy-sky ACA frequency over the study period is apparent in
470 this global dataset, noticeably since 2009. However, this inter-annual variability is not matched
471 in the CALIOP data. The seasonal variation in ACA frequency is observed from year-to-year for

472 both OMI and CALIOP (dashed lines). However, from the **year-to-year variation** lines (showing
473 a percentage change per year), only the OMI daytime cloudy-sky frequency shows a significant
474 increase over this time period (solid lines). The increasing **inter-annual variability** in OMI
475 derived daytime global cloudy-sky ACA frequency, **which is** not apparent in any of the CALIOP
476 derived **global cloudy-sky ACA frequencies**, is troublesome and may be attributed to any of the
477 different sensitivities of the two techniques, including cloud and aerosol optical properties,
478 aerosol-cloud separation distance, and/or deficiencies in the OMI data products. As will be
479 described below, we further investigate several aspects of the observed **increasing in inter-annual**
480 **variability in the OMI derived daytime cloudy-sky global ACA frequency**.

481 Given the unexpected monotonic increase in global ACA frequency derived using OMI
482 AI data over the course of our study, we examine the **inter-annual variability** in the OMI daytime
483 cloudy-sky ACA frequency more closely. Figure 9 indicates a near-zero increase in the seasonal
484 averages during the first few years of the study, with frequencies increasing at a rate of roughly
485 **0.3-0.4%** per year starting in 2009. This time period coincides with the start of OMI data loss
486 due to row anomalies, as mentioned above, leading us to further investigate this as a possible
487 reason for the increase in the observed OMI cloudy-sky ACA frequency. Note that we detected
488 data loss while collocating OMI and CALIOP datasets and found no collocated pixels after 2008;
489 a possible sign that the data loss is likely affecting OMI nadir viewing pixels. This is illustrated
490 in Fig. 10a, which depicts a single swath of OMI AI over the African continent on 1 August 2007
491 where only OMI pixels with valid AI are shown. The data loss affected a large portion of the
492 OMI AI data near the nadir regions of each OMI AI swath, as shown from a swath in 1 June
493 2009 (Fig. 10b).

494 Given that the data loss affects mostly nadir-viewing OMI pixels, OMI AI is evaluated as
495 a function of the OMI sensor's viewing zenith angle (VZA) shown in Fig. 11. All OMI AI pixels
496 for one year (2007) are averaged into one-degree VZA bins. Averaged OMI AI values at the
497 edge of the swath are generally higher by about one AI unit than retrievals taken near the center
498 of the swath. Thus, our analysis, which examines inter-annual variability in the OMI-derived
499 ACA frequency, is compromised due to the viewing geometry bias impacting later years of the
500 OMI aerosol products. The remainder of the paper will focus solely on year to year variation
501 derived from CALIOP ACA frequencies, and no further discussion of OMI AI frequencies will
502 be carried out.

503 Next, AERONET AOD data are used to identify a possible bias in the CALIOP lidar due
504 to potential signal deterioration in the instrument. Figure 12 depicts the year-to-year variation in
505 the clear-sky AOD derived using collocated CALIOP-AERONET data over all coastal and island
506 AERONET stations (Zhang and Reid, 2006). The inter-annual variability in the global AOD
507 similar to those for the collocated AERONET and CALIOP data as shown in Fig. 12 seems to
508 suggest that potential deterioration issue from CALIOP are rather insignificant to our ACA
509 study.

510

511 **6. Sensitivity Study**

512 We next investigate the impact that our noise floor thresholds for overlying CALIOP
513 AOD and/or underlying COD exhibit on derived global CALIOP cloudy-sky ACA frequency.
514 All CALIOP cloud and aerosol layer datasets are reprocessed such that the following conditions
515 are met: (a) the underlying COD is greater than 0.3 and 2.5, respectively, (b) the AOD of the
516 above-cloud aerosol plume is greater than 0, and (c) both conditions (a) and (b) are true.
517 Passive-based radiance retrievals have been shown to lack sensitivities to optically-thin cloud

518 detection for optical depths less 0.3 (Sassen and Cho, 1992; Ackerman et al., 2008; Holz et al.,
519 2008). Thus, restricting the CALIOP COD to this threshold offers a more direct comparison of
520 CALIOP- and OMI-based ACA frequencies. However, given that this range of optical depth
521 corresponds with relatively high cirrus clouds, for which little contribution to the overall sample
522 is expected, and broken low-level liquid phase clouds that are biased to ambiguously low values
523 from signal aggregation effects in the 5-km product (Leahy et al., 2012; Campbell et al., 2015),
524 this higher threshold provides a more representative basis for evaluation. We re-compute the
525 monthly global mean cloudy-sky frequency for each of the CALIOP-constrained samples
526 defined above during both daytime and nighttime. **The inter-annual variability in global cloudy-**
527 **sky ACA frequency derived from CALIOP are shown in Fig. 13.** Corresponding sample sizes
528 and mean global frequencies are shown in Table 2.

529 In comparison with the unfiltered data from the daytime (solid red) and nighttime (dotted
530 red) analyses, the various threshold techniques, including the filtering of CALIOP ACAOD
531 according to our floor noise, correspond with significant variance in our results. However, all
532 sensitivity tests seem to show the same slightly-negative trend in cloudy-sky ACA frequency.
533 Although, those ACA events found over optically thicker clouds ($COD > 2.5$) seem to show
534 more of a null **inter-annual variability** over time rather than a slightly-negative **inter-annual**
535 **variability** in the CALIOP global ACA frequency. The COD threshold tests **raises** the daytime
536 mean global cloudy-sky frequency from **1.8%** to **2.0** and **2.5%** for the 0.3 and 2.5 COD
537 thresholds, respectively. This corresponds with a reduction in the sample size of approximately
538 **0.4** ($COD < 0.3$) and **0.6** ($COD < 2.5$) million scenes when compared to the unfiltered methods.
539 During the nighttime analysis, the global mean cloudy-sky frequency is changed from **4.5%** to
540 **6.1** and **8.1%**, respectively, while data counts change to **2.8** and **2.1** million globally for the

541 corresponding nighttime COD threshold tests. Setting a noise floor threshold on the AOD
542 reduces mean global cloudy-sky ACA frequencies by 0.33 and 1.9% for day and nighttime
543 analyses, respectively, corresponding with a reduction of global data counts of 0.3 and 1.6
544 million scenes. After screening out millions of samples during this sensitivity analysis, the same
545 near-zero or decreasing trend is found for CALIOP ACA frequencies, which is indication that
546 neither cloud or aerosol thresholds, or lack there-of, have a major impact on the inter-annual
547 variability of global CALIOP cloudy-sky ACA frequency.

548

549 7. Regional Year-to-Year Variation Analysis

550 A regional analysis of cloudy-sky ACA frequency is also conducted, consistent with
551 methods described above for global analysis. Regional analyses were chosen over high ACA
552 frequency regions, as indicated from Fig. 3. The nine regions of interest, shown in Table 3 and
553 indicated by the red boxes in Fig. 3, are: Northern Saharan Africa, Southern Africa, Southeast
554 Asia, China, the Middle East, South America, India, North America, and the Southern Oceans.
555 Figure 14 shows the regional cloudy-sky de-seasonalized ACA frequency for CALIOP daytime
556 (blue) and nighttime (teal) analyses, along with linear regression lines (described earlier for the
557 global analysis). Positive inter-annual variability in the cloudy-sky ACA frequency are found
558 over the Middle East and India for both daytime and nighttime. In contrast, decreasing inter-
559 annual variability in the cloudy-sky ACA frequency are found over China and South America for
560 both daytime and nighttime. All other regions correspond with a negligible change in cloudy-
561 sky ACA frequency during the study period. Additionally, a regional analysis of variation of
562 cloud coverage over time is also conducted in order to further investigate whether the observed
563 increases in ACA frequency over time are a result of cloud coverage or aerosol loading, although
564 positive AOD trends are observed from both regions (Zhang and Reid, 2010; Hsu et al., 2012).

565 Cloud cover **frequency** exhibits **an insignificant trend** over India indicating the ACA frequency
566 increase may be due to aerosol loading increase over the region, while the observed increase in
567 cloudy-sky ACA **frequency** over the Middle-East may be also due to the aerosols, as a slight
568 decrease cloud coverage **frequency** is observed **over time** over this region. **Inter-annual**
569 **variability and its significance** are also calculated for each of the regional and global analyses
570 shown in Table 3 using methods described by Weatherhead et al. (1998). As is apparent from
571 Table 3, none of the trends are statistically significant (i.e., trend significance > 2) with a
572 confidence interval of 95%. Applying methods described in Weatherhead et al., (1998), we
573 determine that an ACA data record spanning 37 and 36 years is needed to detect a 1 % yearly
574 change with 95 % confidence, in cloudy-sky ACA frequency for day and nighttime, respectively.

575 **Inter-annual variability** for both ACAOD and cloud-free AOD are also calculated
576 globally and for all regions shown in Table 3. Globally, the **inter-annual variabilities** of clear-sky
577 AOD and **ACAAOD** are slightly positive, while the ACA frequency is **negative** during both day
578 and night. Regions corresponding with a negative trend of all three parameters (ACA frequency,
579 ACAOD, and clear-sky AOD) include: Southeast Asia (nighttime) and South America
580 (nighttime). The Middle East (day and night) and India (day) regions exhibit positive trends for
581 all three parameters. The remaining regions exhibit a combination of positive, negative or near-
582 zero trends in all three parameters.

583

584 **8. Conclusions**

585 Using Cloud-Aerosol Lidar with Orthogonal Polarization (CALIOP) layer products and
586 collocated Ozone Monitoring Instrument (OMI) Aerosol products and Aqua Moderate
587 Resolution Imaging Spectroradiometer (MODIS) cloud products data from June 2006 –
588 December 2013, spatial distributions, including global and regional variabilities, of above cloud

589 aerosol (ACA) events are studied and compared. Active-based profiling is considered an optimal
590 means for identifying ACA occurrence. OMI identification is restricted to ultra-violet (UV)-
591 absorbing ACA events (i.e., smoke), in contrast, through the Aerosol Index (AI) parameter.
592 However, the relatively wide field-of-view of the paired OMI/MODIS datasets, in tandem,
593 provide greater data volume overall, which serves as a relatively well-characterized reference for
594 comparing with CALIOP.

595 The primary findings of this study are:

- 596
- 597 1. Baselines values for the passive-based OMI AI as well an active-based CALIOP
598 above-cloud aerosol optical depth (ACAOD) are established in order to
599 distinguish background noise from signal due to significant ACA events such as
600 dust outbreaks and biomass burning. The “noise floor” for OMI AI and CALIOP
601 are applied to their respective data sets during processing. However, caution
602 should be exercised when using these baselines, as they are an approximation and
603 will vary depending on ancillary observational parameters for OMI and day
604 versus nighttime sensitivity for CALIOP.
 - 605 2. Despite fundamental differences in spatial and vertical samplings, as well as
606 sensitivity to ACA aerosol types, both OMI- and CALIOP-based techniques
607 broadly resolve consistent global/spatial distributions of cloudy-sky ACA
608 frequency. For example, both capture ACA events over the Northwest Coast of
609 Africa and the Arabian Peninsula during the Dec. - May period, and over the
610 North- and South-west Coast, as well as the Southeast Coast of Africa, the
611 Arabian Peninsula and Arabian Sea during the June - Nov. period. Still,
612 discrepancies, as expected, are present. For example, daytime cloudy-sky ACA

613 frequencies of up to 10% are found from CALIOP over Southeast Asia during the
614 June-Nov. period **while** such ACA events are none existent using OMI-based
615 method. Over North Africa, cloudy-sky ACA frequencies of around **20-30%** are
616 reported for both periods from the OMI-based method, yet such events are largely
617 undetected by the CALIOP-based method. We suspect that heavy dust plumes
618 may be misidentified as clouds by the passive-based method, thus causing an
619 unexpected rise in the passive-based derived cloudy-sky ACA frequency over that
620 region.

621 **3. The differences between the OMI- and CALIOP-based daytime cloudy-sky ACA**
622 **frequencies are further explored, using a collocated OMI-MODIS-CALIOP**
623 **dataset for the period of June 2006 – November 2008. Our analysis shows that**
624 **the difference in cloud detectability between the MODIS and CALIOP**
625 **instruments, as well as the QA flags applied, are the major reasons for the**
626 **differences. Although the OMI-MODIS-based method is only sensitive to UV-**
627 **absorbing aerosols and the CALIOP-based method is capable of detecting ACA**
628 **events of all aerosol types, we did not find this to be one of the major reasons for**
629 **the difference in ACA frequencies.**

630 **4. CALIOP nighttime data exhibit slightly larger distributions and a 10-20 % greater**
631 **cloudy-sky ACA frequency annually in comparison to daytime. This may be due**
632 **the subsidence of the planetary boundary layer at night, influencing frequencies of**
633 **low-cloud formation, as well as the impact of higher signal-to-noise in CALIOP**
634 **datasets for subsequent Level 2 analysis partly controlled for in our study by**
635 **applying the noise floor. To the latter point, previous study has shown relative**

636 stability between day/night CALIOP aerosol products (Campbell et al., 2012).
637 However, the implicit effect on the vertical distribution of aerosol occurrence was
638 not specifically investigated. More detailed study is needed to reconcile this
639 finding.

640 5. An analysis shows a near-zero negligible slope in the global CALIOP cloudy-sky
641 and all-sky ACA frequencies. However, OMI-MODIS cloudy-sky daytime ACA
642 frequencies show an increase of $\sim 0.3-0.4$ % / year since 2009, possibly due to a
643 significant loss in the OMI data starting in 2009 mostly for nadir viewing pixels.
644 Investigation of the relationship between OMI Aerosol Index (AI) and satellite
645 viewing zenith angle, suggests a viewing angle dependency of OMI AI.
646 Considering that OMI AI increases near the edge of the viewing swath, it is
647 possible that the overall increase in ACA frequency is due to the significant loss
648 of OMI AI data during later years of the study.

649 6. **Changes** in the cloudy-sky global ACA frequency and data counts ranging from
650 **2-4** % and **1-3** million, respectively, **are found** as a result of applying a variety of
651 thresholds to the ACAOD and/or underlying cloud optical depth (COD) during
652 sensitivity analysis. COD thresholds of 0.3 and 2.5 filter high cirrus clouds and
653 non-contiguous low-level water clouds, respectively. CALIOP data are further
654 reprocessed with no restriction to the ACAOD. Most threshold tests show a
655 reduction in global ACA frequencies however those ACA events located over
656 optically thick clouds (COD > 2.5) show a near zero slope in the ACA frequency
657 variability. However, a significant change over time to CALIOP global day or
658 nighttime ACA frequency is not apparent.

659 7. Globally, clear-sky AOD and ACAOD temporal variations are slightly positive
660 while cloudy-sky ACA frequency exhibits a slightly negative inter-annual
661 variability in both the day and night times. Some select regions examined
662 globally, selected for their relatively high ACA frequency overall, exhibit a
663 consistent inter-annual variability in all three parameters. For example,
664 statistically significant increases in clear sky AOD are found over India and
665 Middle-East from various passive based analysis (e.g. Zhang and Reid, 2010).
666 Increasing in cloudy-sky ACA frequencies are also found for the two regions for
667 the study period of 2006-2013. Other regions exhibit agreement between some,
668 but not all, parameters. However, neither the regional or global trends of any of
669 the three parameters are statistically significant. An ACA data record spanning at
670 least 30 years is needed in order to report a 10% per decade change in ACA
671 frequency with 95% confidence.

672 This study confirms that significant (i.e., resolvable with the techniques applied) ACA
673 events occur with a frequency of 1-8% globally and as high as 30-50 %, regionally, over some of
674 the most ACA-abundant regions. The two complementary techniques applied to locate ACA
675 events and derive global and regional distributions and both exhibit strengths and weaknesses.
676 This study shows that, when used simultaneously, combined passive/active analysis can help
677 present a more comprehensive analysis of ACA than a single-sensor analysis alone. However,
678 the analysis strongly reinforces the use of active-based lidar profiling for distinguishing aerosol
679 presence that perturbs passive-based column-integrated radiative parameters. The vertical
680 distribution and optical properties of aerosol and cloud layers are fundamental to accurate
681 column radiative closure. The effects cloud-aerosol overlap can exhibit on cloud and aerosol

682 property retrieval techniques demands some coordinated active/passive observation for ensuring
683 clarity and limiting bias in top-of-atmosphere retrievals.

684 Due to the extensive spatial coverage and consistency of retrieved datasets from space-
685 borne instruments, trend analyses, and the need for consistent multi-sensor profiling, should
686 become primary motivating factors behind mission design and life expectancy in orbit. Our
687 analysis shows that in a few decades, proper analysis of ACA trends are possible through
688 continuation of a CALIOP/OMI-like paradigm. Ultimately, this work, paired with Alfaro-
689 Contreras (2014) and others, have broadly conceptualized the ACA problem globally. **Past**
690 **studies have shown that ACA events represent a fundamental climate phenomenon on a global**
691 **scale (Peters et al. 2011), thus ACA requires specific long term monitoring.** Trend analysis,
692 then, will help ultimately distinguish this attribute, and thus whether or not ACA is simply noise
693 or a radiatively-significant process that is sensitive to changes in land-use globally and a
694 fluctuating frequency and distribution of elevated aerosol particles over time. Future satellite
695 mission designs should emphasize extending the life of these instruments for application to
696 environmental parameter inter-annual variability studies.

697

698

699 **Acknowledgements**

700 This research is funded through the support of the Office of Naval Research Codes 322.
701 **Author RAC is supported by the NASA project NNX14AJ13G.** Author JRC acknowledges the
702 support of the NASA Interagency Agreement IAARPO201422 on behalf of the CALIPSO
703 Science Team. We thank the AERONET program and their contributing principal investigators
704 for collecting and maintaining the sun-photometer data. CALIOP cloud and aerosol layer data

705 were obtained from the Atmospheric Science Data Center. MODIS cloud data were obtained
706 from the Goddard Space Flight Center Level 1 and atmospheric archive and distribution center
707 system. The OMI aerosol data were obtained from the Goddard Earth Science Data Center and
708 Information Service Center. **We thank Abhay Devasthale, Karsten Peters, Hiren Jethva and two**
709 **other anonymous reviewers for their constructive comments and suggestions.**

710

711

712 **References**

- 713 Ackerman, S.A., Strabala, K.I., Menzel, W.P., Frey, R.A, Moeller, C.C., and Gumley, L.E.:
- 714 Discriminating clear sky from clouds with MODIS, *J.Geophys. Res.*,103(D24),32141-
- 715 32157, doi:10.1029/1998JD200032, 1998.
- 716 Ackerman, S.A., Holz, R.E., Frey, R.E., Eloranta, R.W., Maddux, B., and McGill, M.J.: Cloud
- 717 detection with MODIS: Part II. Validation, *J. Atmos. Oceanic Technol.*, 25, 1073-
- 718 1086.,2008.
- 719 Ackerman, S. A., Frey, R., Strabala, K., Liu, Y., Gumley, L., Baum, B., and Menzel, P.:
- 720 Discriminating clear-sky from cloud with MODIS algorithm theoretical basis document
- 721 (MOD35), ATBD Reference Number: ATBD-MOD-06, 2010.
- 722 Alfaro-Contreras, R., Zhang, J., Reid, J. S., Campbell, J. R., and Holz, R. E.: Evaluating the
- 723 impact of aerosol particles above cloud on cloud optical depth retrievals from MODIS, *J.*
- 724 *Geophys.Res. Atmos.*, 119, 5410–5423, doi:10.1002/2013JD021270, 2014.
- 725 Brioude, J., Cooper, O. R., Feingold, G., Trainer, M., Freitas, S. R., Kowal, D., Ayers, J.K.,Prins,
- 726 E., Minnis, P., McKeen, S. A., Frost, G. J., and Hsie, E.-Y.: Effect of biomass burning on
- 727 marine stratocumulus clouds off the California coast, *Atmos. Chem. Phys.*, 9, 8841–
- 728 8856,doi:10.5194/acp-9-8841-2009, 2009.
- 729 Campbell, J. R., Tackett, J. L., Reid, J. S., Zhang, J., Curtis, C. A., Hyer, E. J., Sessions,W. R.,
- 730 Westphal, D. L., Prospero, J. M., Welton, E. J., Omar, A. H., Vaughan, M. A.,and
- 731 Winker, D. M.: Evaluating nighttime CALIOP 0.532 μm aerosol optical depth and
- 732 extinction coefficient retrievals, *Atmos. Meas. Tech.*, 5, 2143–2160, doi:10.5194/amt-5-
- 733 2143-2012,2012.

734 Campbell, J. R., Vaughan, M. A., Oo, M., Holz, R. E., Lewis, J. R., and Welton, E. J.:
735 Distinguishing cirrus cloud presence in autonomous lidar measurements, *Atmos. Meas.*
736 *Tech.*, 8,435–449, doi:10.5194/amt-8-435-2015, 2015.

737 Chand, D., Anderson, T. L., Wood, R., Charlson, R. J., Hu, Y., Liu, Z., and Vaughan, M.:
738 Quantifying above-cloud aerosol using space borne lidar for improved understanding of
739 cloudy sky direct climate forcing, *J. Geophys. Res.*, 113, D12306,
740 doi:10.1029/2007JD009443, 2008.

741 Chand, D., Wood, R., Anderson, T. L., Satheesh, S. K., and Charlson, R. J.: Satellite-derived
742 direct radiative effect of aerosols dependent on cloud cover, *Nat. Geosci.*, 2, 181–
743 184,doi:10.1038/NGEO437, 2009.

744 Coddington, O. M., Plewskie, P., Redemann, J., Platnick, S., Russell, P. B., Schmidt, K. S.,
745 Gore, W. J., Livingston, J., Wind, G., and Vukicevic, T.: Examining the impact of
746 overlying aerosols on the retrieval of cloud optical properties from passive remote
747 sensing, *J. Geophys.Res.*, 115, D10211, doi:10.1029/2009JD012829, 2010.

748 Devasthale, A. and Thomas, M.A.: A global survey of aerosol-liquid water cloud overlap based
749 on four years of CALIPSO-CALIOP data, *Atmos. Chem. Phys.*, 11,1143-
750 1154,doi:10.519/acp-11-1143-2011, 2011.

751 Eck, T. F., Holben, B. N., Reid, J. S., Dubovik, O., Smirnov, A., O’Neill, N. T., Slutsker, I., and
752 Kinne, S.: Wavelength dependence of the optical depth of biomass burning, urban and
753 desert dust aerosols, *J. Geophys. Res.*, 104, 31333–31349, doi:10.1029/1999JD90093,
754 1999.

755 Haywood, J.M.,Osborne, S.R., and Abel, S.J.: The effect of overlying absorbing aerosol layers
756 on remote sensing retrievals of cloud effective radius and cloud optical depth, *Q.J.R.*
757 *Meteorolog. Soc.*, 130, 779-800. Doi:10.1256/qj.03.100,2004.

758 Holben, B. N., Eck, T. F., Slutsker, I., Tanre, D., Buis, J. P., Setzer, A., Vermote, E., Reagan, J.
759 A.,Kaufman, Y. J., Nakajima, T., Lavenu, F., Jankowiak, I., and Smirnov, A.:
760 AERONET – a federated instrument network and data archive for aerosol
761 characterization, *Remote Sens. Environ.*,66, 1–16, 1998.

762 Holz, R. E., Ackerman, S. A., Nagle, F. W., Frey, R., Dutcher, S., Kuehn, R. E., Vaughan, M. A.,
763 and Baum, B.: Global Moderate Resolution Imaging and Spectroradiometer (MODIS)
764 cloud detection and height evaluation using CALIOP, *J. Geophys. Res.*, 113,
765 D00A19,doi:10.1029/2008JD009837, 2008.

766 Hsu, N. C., Gautam, R., Sayer, A. M., Bettenhausen, C., Li, C., Jeong, M. J., Tsay, S.-C.,and
767 Holben, B. N.: Global and regional trends of aerosol optical depth over land and ocean
768 using SeaWiFS measurements from 1997 to 2010, *Atmos. Chem. Phys.*, 12, 8037–8053,
769 15 doi:10.5194/acp-12-8037-2012, 2012.

770 Intergovernmental Panel on Climate Change (IPCC): The physical science basis, and
771 contribution of working group I to the fourth assessment report of the IPCC 916,
772 Cambridge Univ. Press.,2007

773 Kacenelebogen, M., Redemann, J., Vaughan, M. A., Omar, A. H., Russell, P. B., Burton, S.,
774 Rogers, R. R., Ferrare, R. A., and Hostetler, C. A.: An evaluation of
775 CALIOP/CALIPSO’s aerosol-above-cloud detection and retrieval capability over North
776 America, *J. Geophys. Res. Atmos.*, 119, 230–244, doi:10.1002/2013JD020178, 2014.

777 Kahn, R. A., Garay, M. J., Nelson, D. L., Levy, R. C., Bull, M. A., Diner, D. J., Martonchik, J.
778 V., Hansen, E. G., Remer, L. A., and Tanre, D.: Response to “Toward unified satellite
779 climatology and aerosol properties. 3. MODIS versus MISR AERONET”, *J. Quant.*
780 *Spectrosc. Ra.*, 112, 901–909, doi:10.1016/j.jqsrt.2010.11.001, 2011.

781 Kaufman, Y. J., Remer, L. A., Tanre, D., Li, R. R., Kleidman, R., Mattoo, S., Levy, R., Eck, T.,
782 Holben, B. N., Ichoku, C., Martins, J., and Koren, I.: A critical examination of the
783 residual cloud contamination and diurnal sampling effects on MODIS estimates of the
784 aerosol over ocean, *IEEE T. Geosci. Remote*, 43, 2886–2897, 2005a.

785 Kaufman, Y. J., Koren I., Remer, L.A., Tanre, D., Ginoux, P., and Fan, S.: Dust transport and
786 deposition observed from the Terra-Moderate Resolution Imaging Spectroradiometer
787 (MODIS) spacecraft over the Atlantic Ocean. *J.Geophys.Res.*, 110, D10S12,
788 doi:10.1029/2003JD004436., 2005.

789 King, M. D., Tsay, S. C., Platnick, S. E., Menghua,W., and Liou, K. N.: Cloud retrievals
790 algorithm for MODIS: optical thickness, effective particle radius and thermodynamic
791 phase, Algorithm Theor. Basis Doc. ATBD-MOD-05, NASA Goddard Space Flight
792 Cent., Greenbelt, MD, 1997.

793 Leahy, L. V., Wood, R., Charlson, R. J., Hostetler, C. A., Rogers, R. R., Vaughan, M. A., and
794 Winker, D. M.: On the nature and extent of optically thin marine low clouds, *J. Geophys.*
795 *Res.*, 117, D22201, doi:10.1029/2012JD017929, 2012.

796 Levy, R. C., Mattoo, S., Munchak, L. A., Remer, L. A., Sayer, A. M., Patadia, F., and Hsu, N.
797 C.: The Collection 6 MODIS aerosol products over land and ocean, *Atmos. Meas. Tech.*,
798 6, 2989–3034, doi:10.5194/amt-6-2989-2013, 2013.

799 Li, Z., Zhao, F., Liu, J., Jiang, M., Zhao, C., and Cribb, M.: Opposite effects of absorbing
800 aerosols on the retrievals of cloud optical depth from spaceborne and ground-based
801 measurements, *J. Geophys. Res.-Atmos.*, 119, 5104–5114, doi:10.1002/2013JD021053,
802 2014.

803 Liu, Z., Vaughan, M.A., Winker, D.M., Kittaka, C., Getzewich, B., Kuehn, R., Omar, A., Powell,
804 K., Trepte, C. and Hostetler, C.: The CALIPSO Lidar Cloud and Aerosol Discrimination:
805 Version 2 Algorithm and Initial Assessment of Performance, *J. Atmos. Oceanic Technol.*,
806 26, 1198-1213, 2009.

807 Liu, Z., Winker, D. M., Omar, A. H., Vaughan, M. A., Kar, J., Trepte, C. R., and Hu, Y.:
808 Evaluation of CALIOP 532-nm AOD over clouds, AGU Fall Meeting 2013, 2013.

809 Meyer, K., Platnick, S., Oreopoulos, L., and Lee, D.: Estimating the direct radiative effect of
810 absorbing aerosols overlying marine boundary layer clouds in the southeast Atlantic
811 using MODIS and CALIOP, *J. Geophys. Res. Atmos.*, 118, 4801–4815,
812 doi:10.1002/jgrd.50449, 2013.

813 Peters, K., Quaas, J., and Bellouin, N.: Effects of absorbing aerosols in cloudy skies: a satellite
814 study over the Atlantic Ocean, *Atmos. Chem. Phys.*, 11, 1393–1404, doi:10.5194/acp-11-
815 1393-2011, 2011.

816 Platnick, S., Pincus, R., Wind, B., King, M. D., Gray, M. A., and Hubanks, P.: An initial analysis
817 of the pixel-level uncertainties in the global MODIS cloud optical thickness and effective
818 particle radius size retrievals, *Proc. SPIE 5652, Passive Optical Remote Sensing of the*
819 *Atmosphere and Cloud IV*, 30, doi:10.1117/12.578353, 2004.

820 Powell, K. A., Hostetler, C. A., Liu, Z., Vaughan, M. A., Kuehn, R. E., Hunt, W. H., Lee, K. M.,
821 Trepte, C. R., Rogers, R. R., Young, S. A., and Winker, D. M.: CALIPSO lidar

822 calibration algorithms, part I: Nighttime 532-nm-parallel channel 532-nm perpendicular
823 channel, *J. Atmos. Ocean. Tech.*, 26, 2015–2033, 2009.

824 Remer, L. A., Kaufman, Y. J., Tanre, D., Mattoo, S., Chu, D. A., Martins, J. V., Li, R. R.,
825 Ichoku, C., Levy, R. C., Kleidman, R. G., Eck, T. F., Vermote, E., and Holben, B. N.:
826 The MODIS aerosol algorithm, products and validation. *J. Atmos. Sci.*, 62, 947–973,
827 2005.

828 Remer, L. A., Kleidman, R. G., Levy, R. C., Kaufman, Y. J., Tanre, D., Mattoo, S., Martins, J.
829 V., Ichoku, C., Koren, I., Yu, H., and Holben, B. N.: Global aerosol climatology from
830 MODIS satellite sensors, *J. Geophys. Res.*, 113, D14S07, doi:10.1029/2007JD009661,
831 2008.

832 Roberts, G., Wooster, M. J., and Lagoudakis, E.: Annual and diurnal african biomass burning
833 temporal dynamics, *Biogeosciences*, 6, 849–866, doi:10.5194/bg-6-849-2009, 2009.

834 Rossow, W. B. and Schiffer, R. A.: Advances in understanding clouds from ISCCP, *B. Am.*
835 *Meteorol. Soc.*, 80, 2261–2287, doi:10.1175/1520-
836 04771999:080<2261:AIUCFI>2.0.CO;2, 1999.

837 Royal Netherlands Meteorological Society: Background information about Row Anomaly in
838 OMI, available at: www.knmi.nl/omi/research/product/rowanomaly-background.php,
839 accessed on December 22 2014

840 Sassen, K. and Cho, B. S.: Subvisual-thin cirrus lidar dataset for satellite verification and
841 climatological research, *J. Appl. Meteorol.*, 31, 1275–1285, 1992.

842 Satheesh, S. K., Morthy, K. K., Kaufman, Y. J., and Takemura, T.: Aerosol optical depth,
843 physical properties and radiative forcing over the Arabian Sea, *Meteorol. Atmos. Phys.*,
844 91, 45–62, 2006.

845 Sayer, A. M., Hsu, N. C., Bettenhausen, C., Ahmad, Z., Holben, B. N., Smirnov, A., Thomas, G.
846 E., and Zhang, J.: SeaWiFS Ocean Aerosol Retrievals (SOAR): algorithm, validation,
847 and comparison with other datasets, *J. Geophys. Res.*, 117, D03206,
848 doi:10.1029/2011JD016599, 2012.

849 Schrage, J. M. and Fink, A. H.: Nocturnal continental low-level stratus over Tropical West
850 Africa: observations and possible mechanisms controlling its onset, *Mon. Weather Rev.*,
851 140, 1794– 1809, doi:10.1175/MWR-D-11-00172.1, 2012.

852 Shi, Y., Zhang, J., Reid, J. S., Holben, B., Hyer, E. J., and Curtis, C.: An analysis of the
853 collection 5 MODIS over-ocean aerosol optical depth product for its implication in
854 aerosol assimilation, *Atmos. Chem. Phys.*, 11, 557–565, doi:10.5194/acp-11-557-2011,
855 2011.

856 Smirnov, A., Holben, B. N., Giles, D. M., Slutsker, I., O'Neill, N. T., Eck, T. F., Macke, A.,
857 Croot, P., Courcoux, Y., Sakerin, S. M., Smyth, T. J., Zielinski, T., Zibordi, G., Goes, J.
858 I., Harvey, M. J., Quinn, P. K., Nelson, N. B., Radionov, V. F., Duarte, C. M., Losno, R.,
859 Sciare, J., Voss, K. J., Kinne, S., Nalli, N. R., Joseph, E., Krishna Moorthy, K., Covert,
860 D. S., Gulev, S. K., Milinevsky, G., Larouche, P., Belanger, S., Horne, E., Chin, M.,
861 Remer, L. A., Kahn, R. A., Reid, J. S., Schulz, M., Heald, C. L., Zhang, J., Lapina, K.,
862 Kleidman, R. G., Griesfeller, J., Gaitley, B. J., Tan, Q., and Diehl, T. L.: Maritime
863 aerosol network as a component of AERONET – first results and comparison with global
864 aerosol models and satellite retrievals, *Atmos. Meas. Tech.*, 4, 583–597,
865 doi:10.5194/amt-4-583-2011, 2011.

866 Stephens, G. L., Vane, D. G., Boain, R. J., Mace, G. G., Sassen, K., Wang, Z., Illingsworth, A. J.,
867 O'Connor, E. J., Rossow, W. B., Durden, S. L., Miller, S. D., Austin, R. T., Benedetti,

868 A., and Mitrescu, C.: The Cloudsat mission and the A-Train, *B. Am. Meteorol. Soc.*, 83,
869 1771–1790, doi:10.1175/BAMS-83-12-1771, 2002.

870 Stevens, B. and Fetingold, G.: Untangling aerosol effects on clouds and precipitation in a
871 buffered system, *Nature*, 461, 607–613, 2009.

872 Thomason, L. W., Pitts, M. C., and Winker, D. M.: CALIPSO observations of stratospheric
873 aerosols: a preliminary assessment, *Atmos. Chem. Phys.*, 7, 5283–5290, doi:10.5194/acp-
874 7-5283-2007, 2007.

875 Torres, O., Bhartia, P. K., Herman, J. R., and Ahmad, Z.: Derivation of aerosol properties from
876 satellite measurements of backscattered ultraviolet radiation: theoretical basis, *J.*
877 *Geophys. Res.*, 103, 17110, doi:10.1029/98JD00900, 1998.

878 Torres, O., Tanskanen, A., Viehmann, B., Ahn, C., Braak, R., Bhartia, P. K., Veefkind, P., and
879 Levelt, P.: Aerosols and surface UV products from Ozone Monitoring observations: an
880 overview, *J. Geophys. Res.*, 112, D24S47, doi:10.1029/2007JD008809, 2007.

881 Torres, O., Jethva, H., and Bhartia, P. K.: Retrieval of aerosol optical depth above clouds from
882 OMI observations: sensitivity analysis and case studies. *J. Atmos. Sci.*, 69, 1037–1053,
883 2012.

884 Waquet, F., Reidi, J., Labonnote, L. C., Goloub, P., Cairns, B., Deuze, J. L., and Tanre, D.:
885 Aerosol remote sensing over clouds using A-train observations, *J. Atmos. Sci.*, 66, 2468–
886 2480, 2009.

887 Weatherhead, E. C., Reinsel, G. C., Tiao, G. C., Meng, X. L., Choi, D., Cheang, W. K., Keller,
888 T., DeLuisi, J., Wuebbles, D. J., Kerr, J. B., Miller, A. J., Oltmans, S. J., and Frederick, J.
889 E.: Factors affecting the detection of trends: statistical considerations and applications to
890 environmental data, *J. Geophys. Res.*, 103, 17149–17161, 1998.

891 Wetherald, R. T. and Manabe, S.: Cloud feedback processes in a general circulation model J.
892 Atmos. Sci., 45, 1397–1415, 1988.

893 Wilcox, E. M.: Direct and semi-direct radiative forcing of smoke aerosols over clouds, Atmos.
894 Chem. Phys., 12, 139–149, doi:10.5194/acp-12-139-2012, 2012.

895 Wilcox, E. M., Harshvardian and Platnick, S.: Estimate of the impact of absorbing aerosol over
896 cloud on the MODIS retrievals of cloud optical thickness and effective radius using two
897 independent retrievals of liquid water path, J. Geophys. Res., 114, D05210,
898 doi:10.1029/2008JD010589, 2009.

899 Winker, D. M., Vaughan, M. A., Omar, A. H., Hu, Y., Powell, K. A., Liu, Z., Hunt, W. H., and
900 Young, S. A.: Overview of the CALIPSO mission and CALIOP data processing
901 Algorithm. J. Atmos. Ocean. Tech., 26, 2310–2323, doi:10.1175/2009TECHA.1281.1,
902 2009.

903 Winker, D. M. and coauthors.: The CALIPSO mission: a global 3D view of aerosols and clouds,
904 B. Am. Meteorol. Soc., 91, 1211–1229, 2010.

905 Wood, R.: Stratocumulus clouds, Mon. Weather Rev., 140, 2373–2423, 2012.

906 Yu, H., Dickinson, R., Chin, M., Kaufman, Y., Holben, B., Geogdzhayev, I., and Mischenko, M.:
907 Annual cycle of global distributions of aerosol optical depth from integration of MODIS
908 retrievals and GOCART model simulations, J. Geophys. Res., 108, 4128,
909 doi:10.1029/2002JD002717, 2003.

910 Yu, H., Zhang, Y., Chin, H., Liu, Z., Omar, A., Remer, L. A., Yang, Y., Yuan, T., and Zhang, J.:
911 An integrated analysis of aerosols above-clouds from A-train multi sensor measurements,
912 Remote Sens. Environ., 121, 125–131, 2012.

913 Zhang, J., Christopher, S. A., and Holben, B. N.: Intercomparison of smoke aerosol optical
914 thickness derived from GOES 8 imager and ground-based Sun photometers, *J. Geophys.*
915 *Res.*, 106, 7387–7397, doi:10.1029/2000JD900540, 2001.

916 Zhang, J. and Reid, J. S.: MODIS aerosol product analysis for data assimilation: assessment of
917 level 2 aerosol optical thickness retrievals, *J. Geophys. Res.*, 111, D222077,
918 doi:10.1029/2005JD006898, 2006.

919 Zhang, J. and Reid, J. S.: A decadal regional and global trend analysis of the aerosol optical
920 depth using a data-assimilation grade over-water MODIS and Level 2 MISR aerosol
921 products, *Atmos. Chem. Phys.*, 10, 10949–10963, doi:10.5194/acp-10-10949-2010, 2010.

922 Zhang, J., Campbell, J. R., Reid, J. S., Westphal, D. L., Baker, N. L., Campbell, W. F., and Hyer,
923 E. J.: Evaluating the impact of assimilating CALIOP-derived aerosol extinction profiles
924 on a global mass transport model, *Geophys. Res. Lett.*, 38, L14801,
925 doi:10.1029/2011GL047737, 2011.

926 Zhang, J., Reid, J. S., Campbell, J. R., Hyer, E. J., and Westphal, D. L.: Evaluating the impact of
927 multi-sensor data assimilation on a global aerosol particle transport model, *J. Geophys.*
928 *Res. Atmos.*, 119, 4674–4689, doi:10.1002/2013JD020975, 2014.

929 Zhang, Z., Meyer, K., Platnick, S., Oreopoulos, L., Lee, D., and Yu, H.: A novel method for
930 estimating shortwave direct radiative effect of above-cloud aerosols using CALIOP and
931 MODIS data, *Atmos. Meas. Tech.*, 7, 1777–1789, doi:10.5194/amt-7-1777-2014, 2014.

932

Figure Captions

Figure 1. (A-H) Multi-year (2006-2013) CALIOP-derived daytime global cloudy-sky ACA frequency applying different CALIOP AODs as the threshold between background and significant aerosol loading. The CALIOP AOD are binned into $2.5^\circ \times 2.5^\circ$ bins derived using the CALIOP cloud and layer data sets. CALIOP AOD baseline thresholds of 0, 0.010, 0.015 and 0.020 are applied to Figs. 1A, 1B, 1C and 1D respectively for the Dec.-May period. Figures 1E-1H show the similar results as Fig. 1A-1D but for the June-Nov. period.

Figure 2. (A) Pairwise comparison between collocated OMI and CALIOP observations of above-cloud AI and AOD, respectively, as a function of the underlying MODIS cloud optical depth (COD). CALIOP AOD are averaged into OMI AI bins of 0.1. (B-I) Multi-year (2006-2013) daytime global cloudy-sky ACA frequency applying several different OMI AIs as the threshold between background and significant aerosol loading. The OMI AIs are binned into $1^\circ \times 1^\circ$ bins derived from the MODIS-OMI collocated data set. OMI AI baseline thresholds of 0.7, 0.8, 0.9 and 1.0 are applied to Figs. 2B, 2C, 2D and 2E respectively for the Dec.-May period. Figures 2F-2I depict the same information as Figs. 2B-2E for the June-Nov. period. ACA frequencies less than 5 % are shown in white.

Figure 3. (A) Seven year (December 2006- May 2013) daytime cloudy-sky frequency of occurrence of aerosol above-cloud events during December through May defined from OMI (ratio of **totally cloudy** MODIS pixels with AI greater than 1.0 to the number of **totally cloudy** MODIS pixels). (B) Day-time cloudy-sky frequency of occurrence of ACA events over cloudy skies from CALIOP (ratio of CALIOP pixels with $\text{CALIOP AOD}_{\text{above cloud}} > 0.015$ to the number of CALIOP pixels with column integrated $\text{COD} > 0$) for the

same temporal domain as Fig. 3A. (C) Night-time cloudy-sky frequency of occurrence defined similar to the daytime frequency from Fig. 3B. (D-F) Shows the same information as Figs. 3A-3C during June 2006-November 2013. Figures 3G-3H depict the ACA frequency ratio defined as the OMI-MODIS daytime cloudy-sky frequency divided by the CALIOP derived daytime cloudy-sky frequency for the December to May and June to November period, respectively. Figures 3I-3J depict the difference in cloudy-sky frequency used to construct the frequency ratio plots (3G and 3H) for the same temporal ranges. The red boxes show the areas selected for regional studies. Only OMI and CALIOP bins with frequency of 5% or higher are shown in this analysis.

Figure 4. (A) Multi-year (2006-2013) daytime AI averaged into $1.0^\circ \times 1.0^\circ$ bins constructed from collocated MODIS and OMI AI over strictly MODIS cloudy scenes during December through May. The averaged OMI AI is neglected below 1.0 in accordance with the AI ground floor determined in Fig. 2. (B) Multi-year (2006-2013) daytime ACAOD averaged into $2.5^\circ \times 2.5^\circ$ bins derived from CALIOP cloud and aerosol layer products. Averaged CALIOP ACAOD below 0.015 are considered below the noise floor for the study and thus are not shown. (C) Shows the CALIOP ACAOD similar to Fig. 4B except for night-time observations. (D-F) Shows the same information as Figs. 4A-4C during the summer and fall months (June-November).

Figure 5. Multi-year (June 2006 - November 2013) frequency of occurrence of low-level clouds defined by CALIOP as the ratio of pixels with COD greater than 0 with cloud-top height $< 3\text{km}$ to the total number of CALIOP scenes within the current $2.5^\circ \times 2.5^\circ$ bin for (A) December to May during daytime observations, (B) December to May of night-time observations, (C) Daytime frequency of occurrence of low-level cloud decks defined

similar to Fig 5A. during the June-November time frame and (D). Nighttime frequency of occurrence of low-level cloud decks for the same time frame as Fig. 5C. Figures 5E and 5F depict the night to daytime frequency ratio for the December to May and June to November periods, respectively.

Figure 6. Multi-year (2006-2013) $2.5^\circ \times 2.5^\circ$ averaged CALIOP day-time AOD for (A) December through May over completely cloud free scenes derived from CALIOP cloud and aerosol layer daytime analysis, (B) Nighttime analysis during the December to May period, (C) Daytime analysis for the June to November period and (D) nighttime analysis for the June to November period. Only scenes which contained an averaged AOD > 0.2 with a column COD = 0 were used in the analysis.

Figure 7. (A) Two-and-a-half-year (June 2006 – November 2008) daytime CALIOP cloudy-sky ACA frequency during the December through May period, using the collocated OMI-MODIS-CALIOP dataset (defined in Table 1). (B) The same as Fig. 7A, however for the all-sky CALIOP ACA frequency. (C) CALIOP cloudy sky frequency, which is defined as the number of collocated CALIOP observations with COD > 0 over the total number of collocated CALIOP observations. (D-F) Similar to Figs. 7a-7c but using the OMI-MODIS-based method (defined in Table 1). (G-J) Depict the same information as 7A-F except for the June – November (2006-2008) period.

Figure 8. (A) Two-and-a-half-year (June 2006 – November 2008) daytime CALIOP cloudy-sky frequency during the December through May period, using the collocated OMI-MODIS-CALIOP dataset with the application of the most lenient cloud QA. (B-C) Depict the same information as Fig. 8A, however now using intermediate and strict cloud QA settings, respectively. (D) Depicts the all-sky frequency using the same

data set as Fig. 8A, now using lenient cloud and aerosol QAs. (E-F) Depict the same information as Fig. 8D varying the cloud QA to intermediate and strict. (G-I) Similar to Figs. D-F but holding the lenient cloud QA while varying the aerosol QA from lenient to intermediate and strict, respectively. (J-R) Depict the same information as Figs. 8A-I for the June to November period (2006 – 2008).

Figure 9. Monthly-averaged global ACA frequencies derived using the OMI-MODIS based method (green) as well as the CALIOP-based method as described in the text. The corresponding baseline thresholds are applied to both CALIOP and OMI data. Dashed lines represent monthly variations in ACA frequencies and the solid lines represent the yearly ACA frequency trends: OMI daytime cloudy-sky frequency is shown in green, CALIOP nighttime cloudy-sky frequency is orange, CALIOP nighttime all-sky frequency is purple, CALIOP daytime cloudy-sky frequency is red and CALIOP daytime all-sky frequency is blue.

Figure 10. (A) A single swath from the OMI instrument over northern Africa on August 1, 2007 before the significant data loss reported in all OMI aerosol products. (B) A single OMI AI swath over the same region as Fig. 10A on June 1, 2009 which is affected by the significant data loss.

Figure 11. The OMI AI as a function of the sensor's viewing zenith angle (VZA). All OMI AI data over the course of a year (2007) were binned into 1° VZA increments. The red vertical bars represent the 95% confidence interval for each 1° bin.

Figure 12. Monthly-averaged over ocean clear-sky AODs derived from collocated CALIOP and AERONET data. CALIOP retrievals within 0.3° latitude and longitude and ± 30 minutes of the corresponding AERONET station and observation are considered collocated.

AERONET and CALIOP AODs above 0.2 and 0.6, respectively, are not included in order to avoid high aerosol loading cases and exclude noisy CALIOP data.

Figure 13. Monthly-averaged global CALIOP cloudy-sky frequencies after applying several different threshold techniques to both day and night time data. The solid lines show the daytime scenario for each respective case while the dotted lines show the nighttime observations for each case.

Figure 14. The de-seasonalized monthly- and regionally-averaged cloudy-sky frequency of ACA occurrences for the nine different regions outlined in Fig. 3 and explained in Table 3. The dashed lines show the monthly frequency over the regions and the solid lines show the trend lines computed for each region with the x-axis representing the year of the study. The CALIOP nighttime analysis is shown in aqua marine and the day-time analysis is shown in dark blue.

Table Captions

Table 1. Various definitions of frequency of above-cloud aerosols (ACA) used throughout the study.

Table 2. Global cloudy-sky relative frequency and data counts for the sensitivity test carried out in Sect. 5. Aerosol and cloud layers retrieved with ‘intermediate’ or ‘strict’ QA metrics are considered in this analysis. A total of five different threshold tests are applied to both day and nighttime CALIOP cloud and aerosol layer products.

Table 3 Seven and a half year above-cloud aerosol cloudy-sky frequency, ACAOD and clear-sky AOD inter-annual variability analysis for the selected target regions. Aerosol and cloud layers retrieved with ‘intermediate’ or ‘strict’ QA metrics are considered in this analysis. Yearly variation for the entire globe is also included. For each region, inter-annual variability (frequency change per year) for the three parameters, the ACA cloudy-sky frequency, ACAOD and clear-sky AOD values are reported. Note that the inter-annual variability for clear sky AODs is estimated using 100% cloud free data from the CALIOP cloud and aerosol layer products.

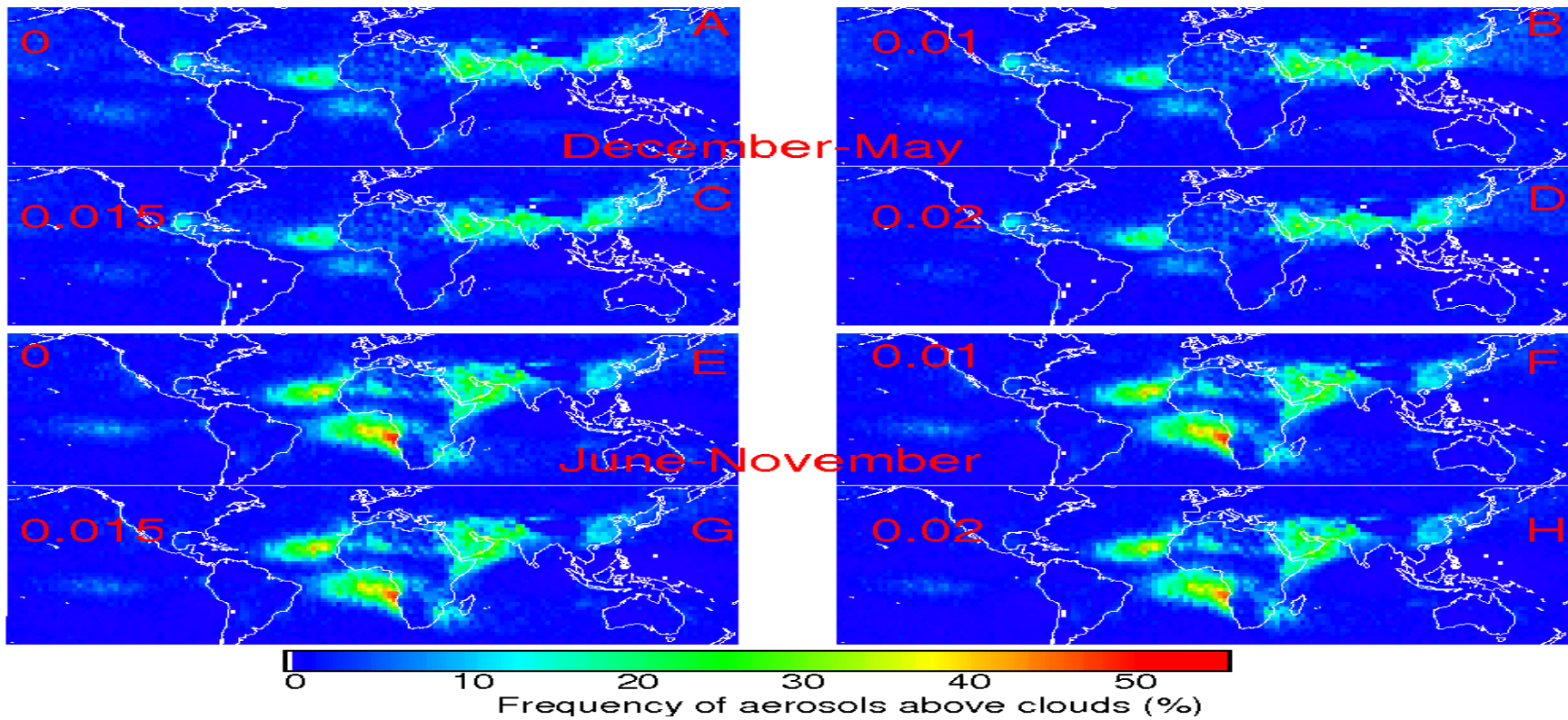


Figure 1. (A-H) Multi-year (2006-2013) CALIOP-derived daytime global cloudy-sky ACA frequency applying different CALIOP AODs as the threshold between background and significant aerosol loading. The CALIOP AOD are binned into $2.5^\circ \times 2.5^\circ$ bins derived using the CALIOP cloud and layer data sets. CALIOP AOD baseline thresholds of 0, 0.010, 0.015 and 0.020 are applied to Figs. 1A, 1B, 1C and 1D respectively for the Dec.-May period. Figures 1E-1H show the similar results as Fig. 1A-1D but for the June-Nov. period.

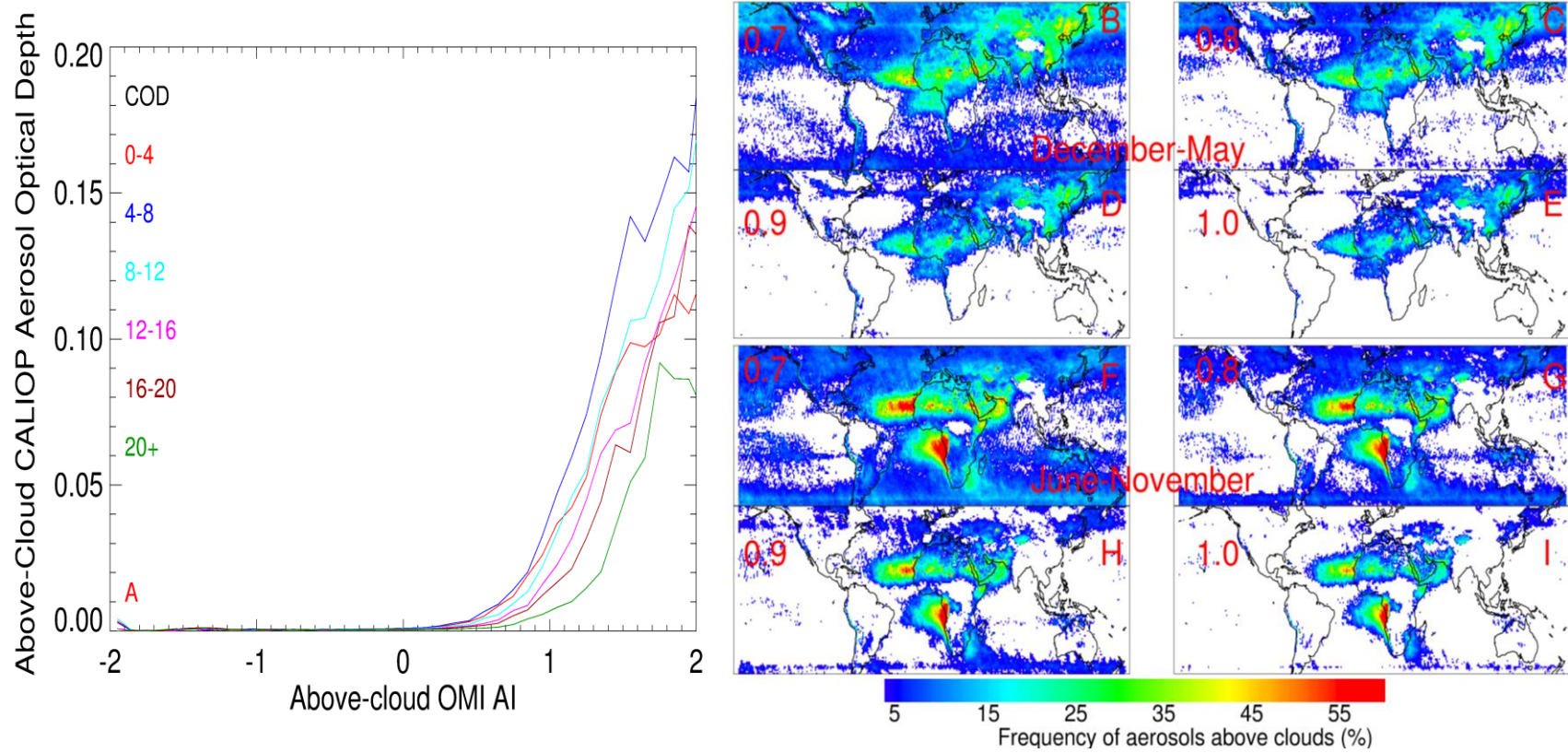


Figure 2. (A) Pairwise comparison between collocated OMI and CALIOP observations of above-cloud AI and AOD, respectively, as a function of the underlying MODIS cloud optical depth (COD). CALIOP AOD are averaged into OMI AI bins of 0.1. (B-I) Multi-year (2006-2013) daytime global cloudy-sky ACA frequency applying several different OMI AIs as the threshold between background and significant aerosol loading. The OMI AIs are binned into $1^{\circ} \times 1^{\circ}$ bins derived from the MODIS-OMI collocated data set. OMI AI baseline thresholds of 0.7, 0.8, 0.9 and 1.0 are applied to Figs. 2B, 2C, 2D and 2E respectively for the Dec.-May period. Figures 2F-2I depict the same information as Figs. 2B-2E for the June-Nov. period. ACA frequencies less than 5 % are shown in white.

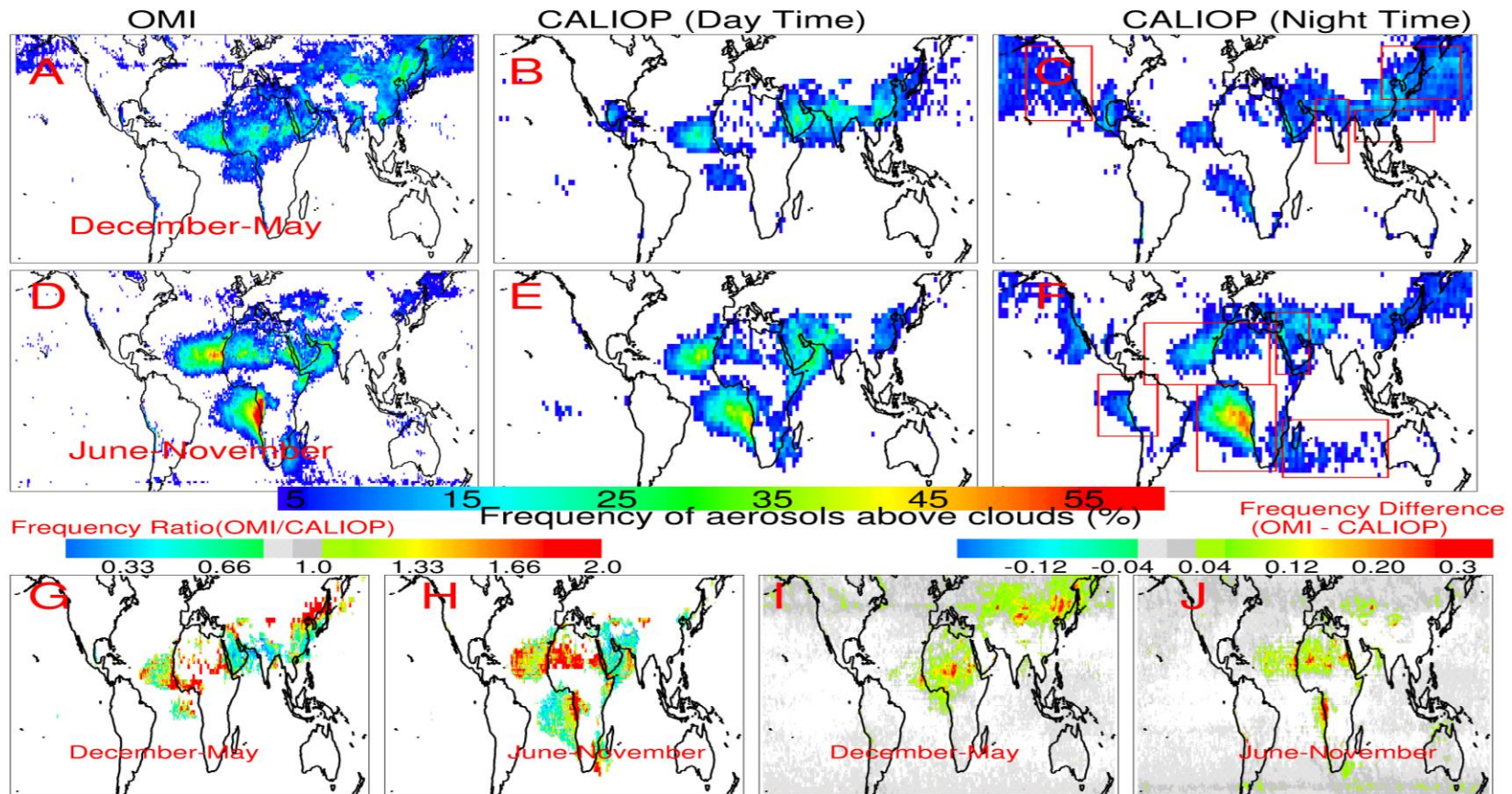


Figure 3. (A) Seven year (December 2006- May 2013) daytime cloudy-sky frequency of occurrence of aerosol above-cloud events during December through May defined from OMI (ratio of **totally cloudy** MODIS pixels with AI greater than 1.0 to the number of **totally cloudy** MODIS pixels). (B) Day-time cloudy-sky frequency of occurrence of ACA events over cloudy skies from CALIOP (ratio of CALIOP pixels with CALIOP $AOD_{above\ cloud} > 0.015$ to the number of CALIOP pixels with column integrated COD > 0) for the same temporal domain as Fig. 3A. (C) Night-time cloudy-sky frequency of occurrence defined similar to the daytime frequency from Fig. 3B. (D-F) Shows the same information as Figs. 3A-3C during June 2006-November 2013. Figures 3G-3H depict the ACA frequency ratio defined as the OMI-MODIS daytime cloudy-sky frequency divided by the CALIOP derived daytime cloudy-sky frequency for the December to May and June to November period, respectively. Figures 3I-3J depict the difference in cloudy-sky frequency used to construct the frequency ratio plots (3G and 3H) for the same temporal ranges. The red boxes show the areas selected for regional studies. Only OMI and CALIOP bins with frequency of 5% or higher are shown in this analysis.

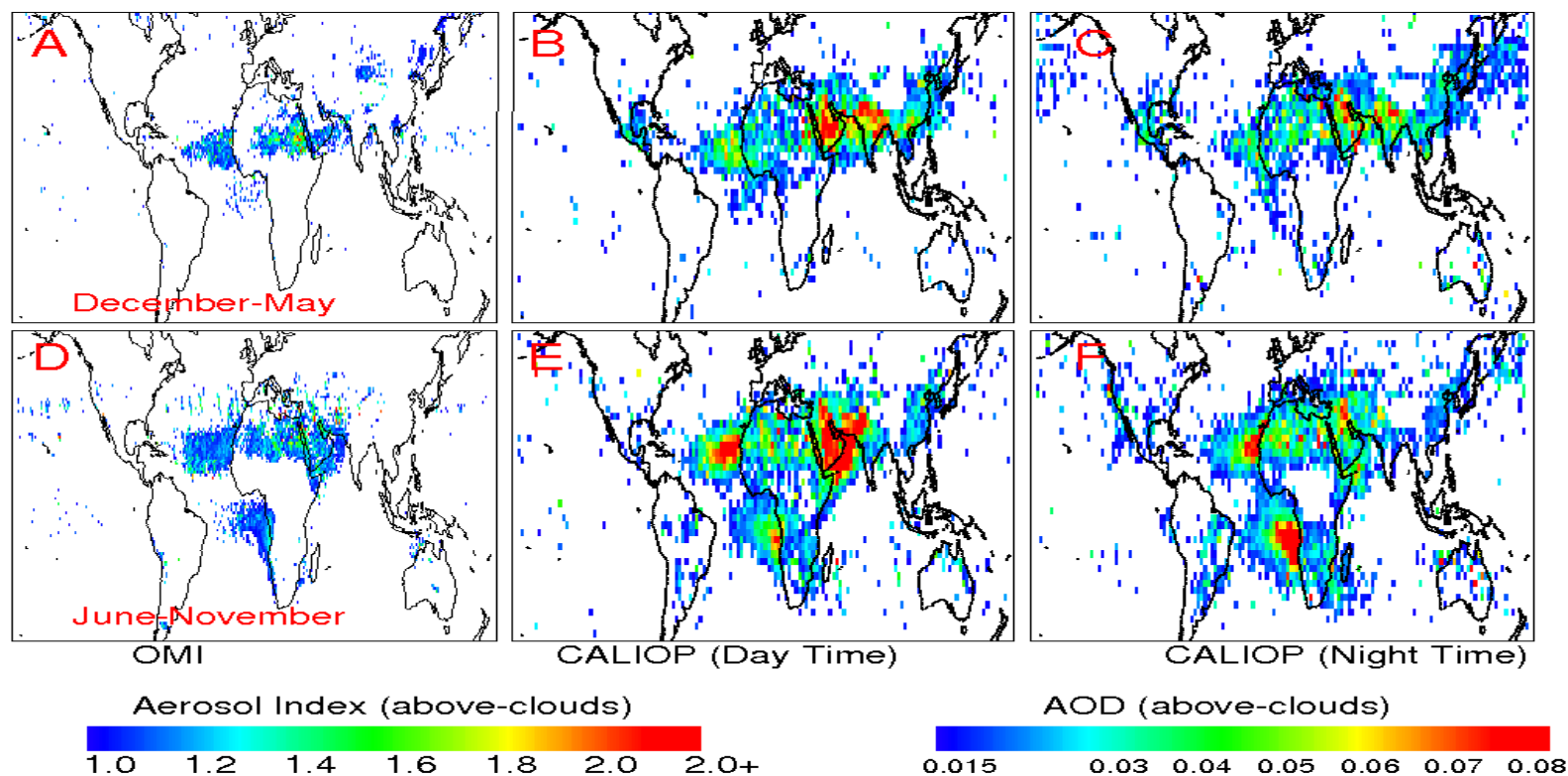
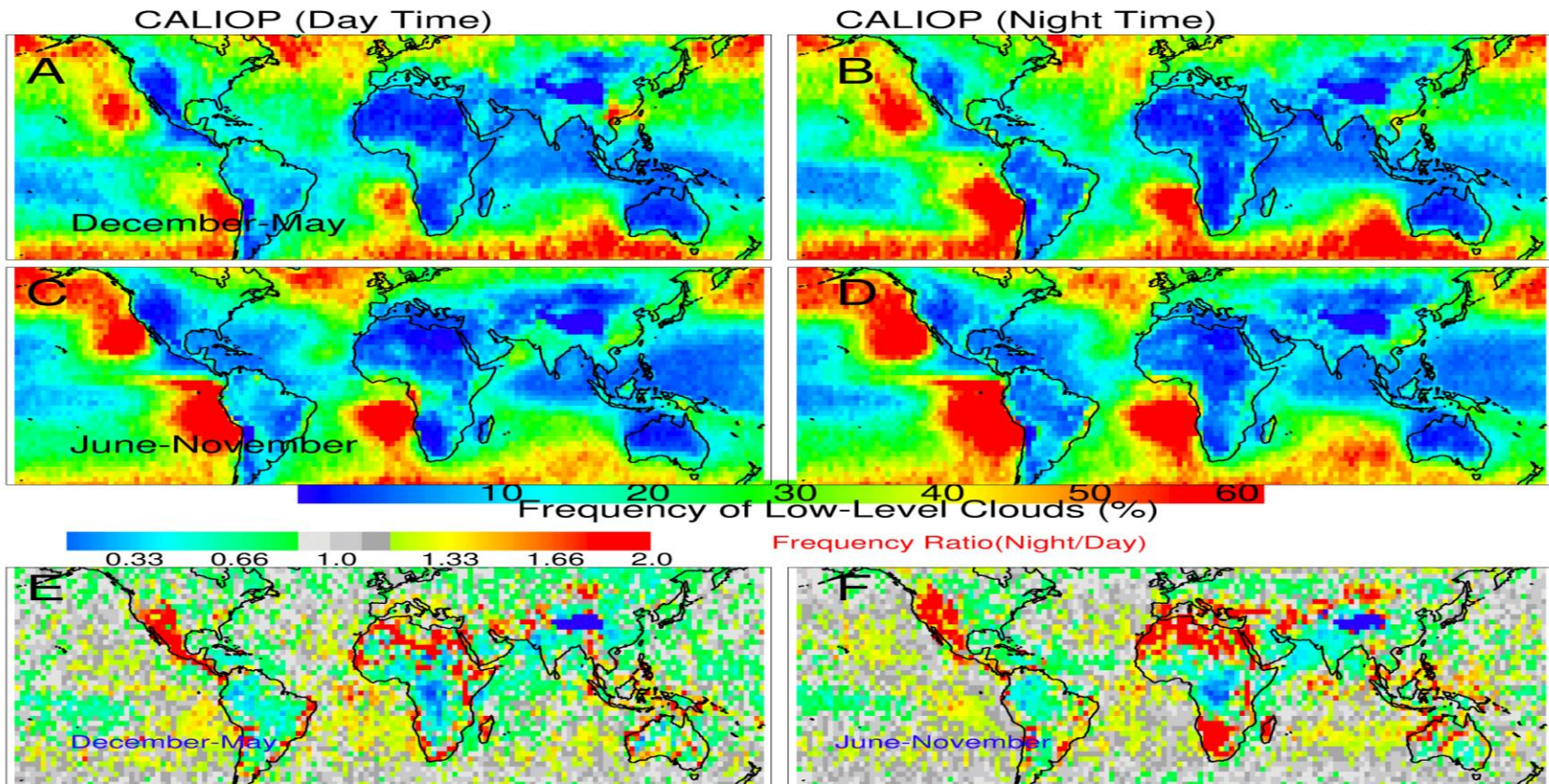


Figure 4. (A) Multi-year (2006-2013) daytime AI averaged into $1.0^\circ \times 1.0^\circ$ bins constructed from collocated MODIS and OMI AI over strictly MODIS cloudy scenes during December through May. The averaged OMI AI is neglected below 1.0 in accordance with the AI ground floor determined in Fig. 2. (B) Multi-year (2006-2013) daytime ACAOD averaged into $2.5^\circ \times 2.5^\circ$ bins derived from CALIOP cloud and aerosol layer products. Averaged CALIOP ACAOD below 0.015 are considered below the noise floor for the study and thus are not shown. (C) Shows the CALIOP ACAOD similar to Fig. 4B except for night-time observations. (D-F) Shows the same information as Figs. 4A-4C during the summer and fall months (June-November).



p9

Figure 5. Multi-year (June 2006 - November 2013) frequency of occurrence of low-level clouds defined by CALIOP as the ratio of pixels with COD greater than 0 with cloud-top height < 3km to the total number of CALIOP scenes within the current 2.5° x 2.5° bin for (A) December to May during daytime observations, (B) December to May of night-time observations, (C) Daytime frequency of occurrence of low-level cloud decks defined similar to Fig 5A. during the June-November time frame and (D). Nighttime frequency of occurrence of low-level cloud decks for the same time frame as Fig. 5C. Figures 5E and 5F depict the night to daytime frequency ratio for the December to May and June to November periods, respectively.

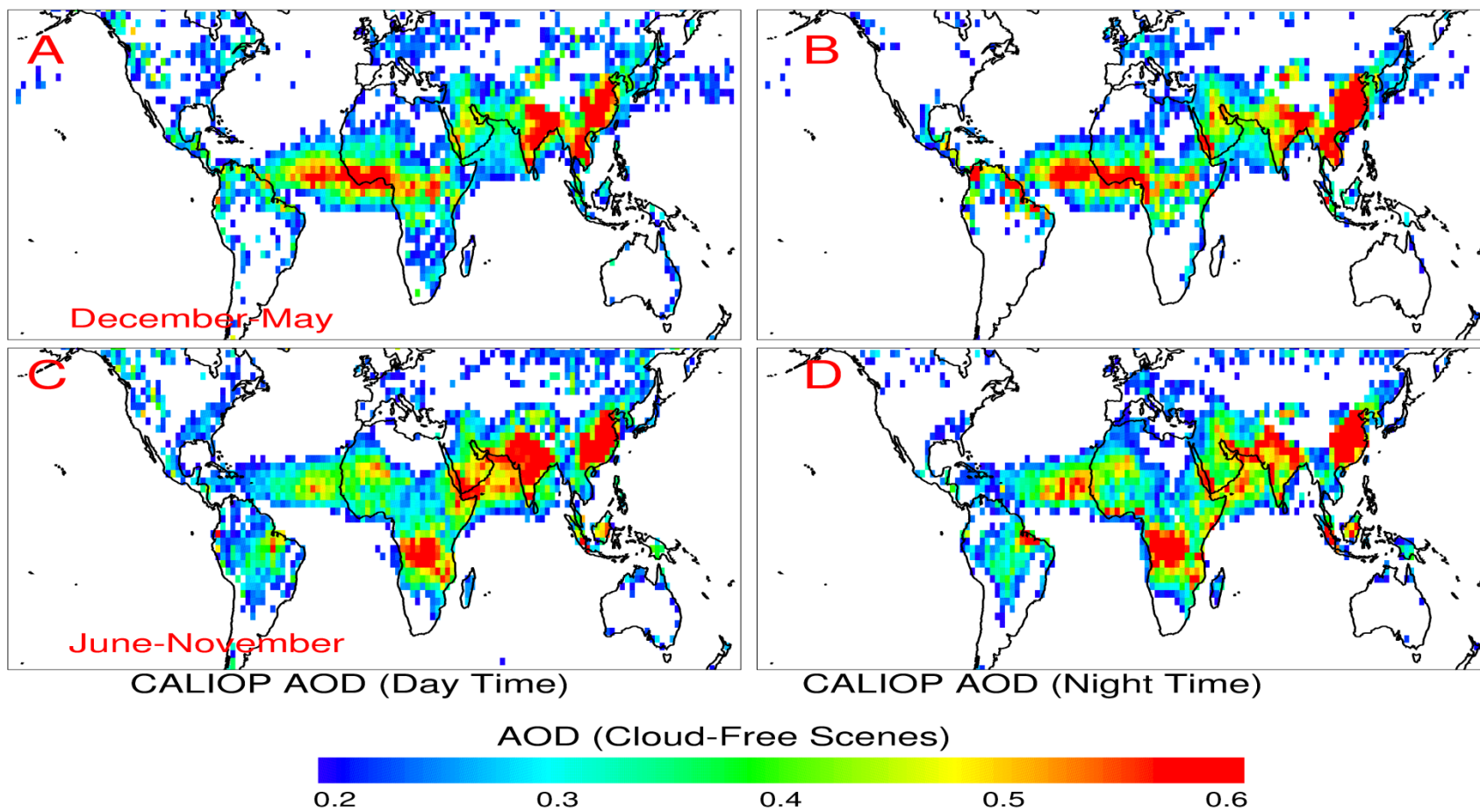


Figure 6. Multi-year (2006-2013) $2.5^\circ \times 2.5^\circ$ averaged CALIOP day-time AOD for (A) December through May over completely cloud free scenes derived from CALIOP cloud and aerosol layer daytime analysis, (B) Nighttime analysis during the December to May period, (C) Daytime analysis for the June to November period and (D) nighttime analysis for the June to November period. Only scenes which contained an averaged AOD > 0.2 with a column COD = 0 were used in the analysis.

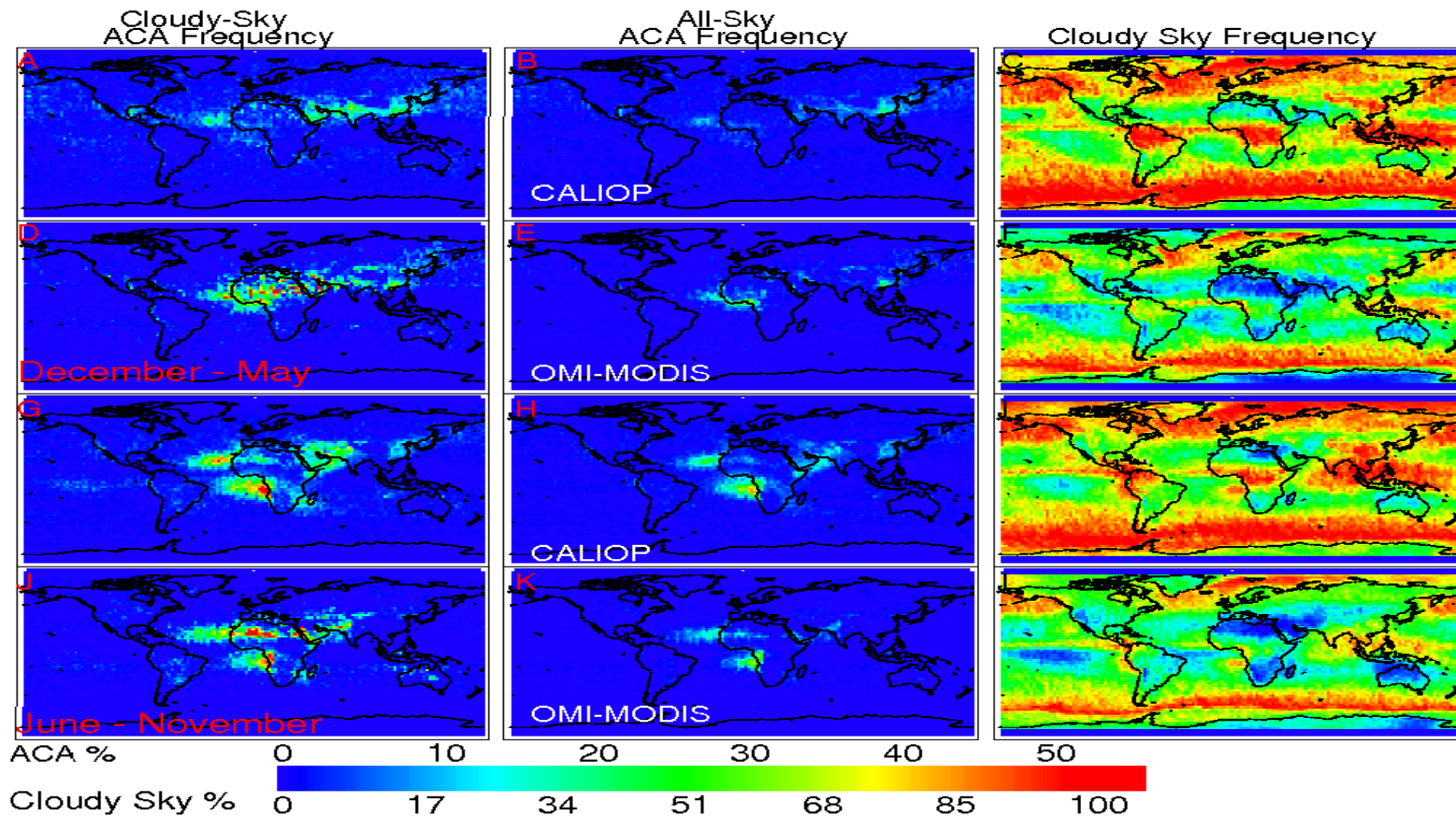


Figure 7. (A) Two-and-a-half-year (June 2006 – November 2008) daytime CALIOP cloudy-sky ACA frequency during the December through May period, using the collocated OMI-MODIS-CALIOP dataset (defined in Table 1). (B) The same as Fig. 7A, however for the all-sky CALIOP ACA frequency. (C) CALIOP cloudy sky frequency, which is defined as the number of collocated CALIOP observations with COD > 0 over the total number of collocated CALIOP observations. (D-F) Similar to Figs. 7a-7c but using the OMI-MODIS-based method (defined in Table 1). (G-J) Depict the same information as 7A-F except for the June – November (2006-2008) period.

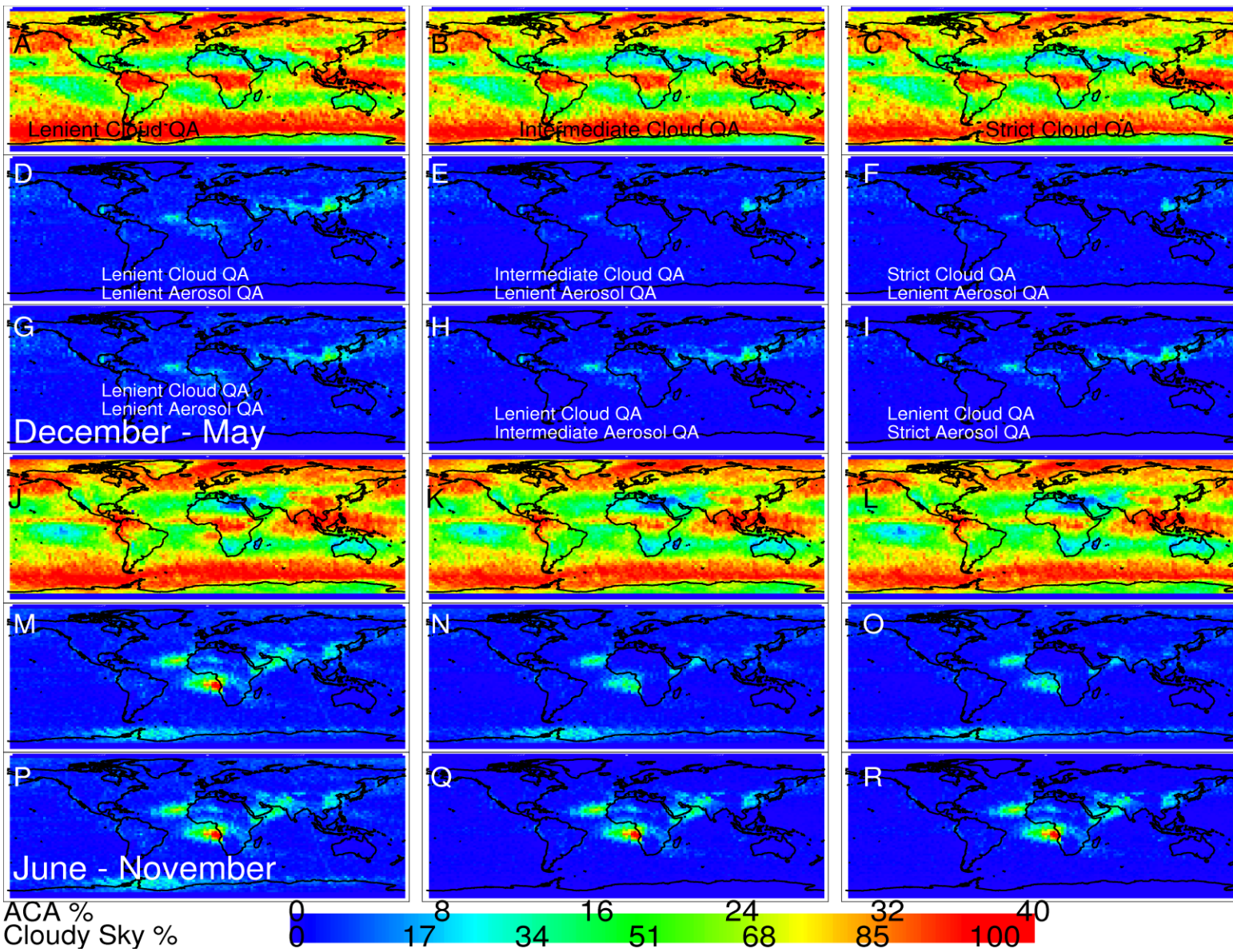


Figure 8. (A) Two-and-a-half-year (June 2006 – November 2008) daytime CALIOP cloudy-sky frequency during the December through May period, using the collocated OMI-MODIS-CALIOP dataset with the application of the most lenient cloud QA. (B-C) Depict the same information as Fig. 8A, however now using intermediate and strict cloud QA settings, respectively. (D) Depicts the all-sky frequency using the same data set as Fig. 8A, now using lenient cloud and aerosol QAs. (E-F) Depict the same information as Fig. 8D varying the cloud QA to intermediate and strict. (G-I) Similar to Figs. D-F but holding the lenient cloud QA while varying the aerosol QA from lenient to intermediate and strict, respectively. (J-R) Depict the same information as Figs. 8A-I for the June to November period (2006 – 2008).

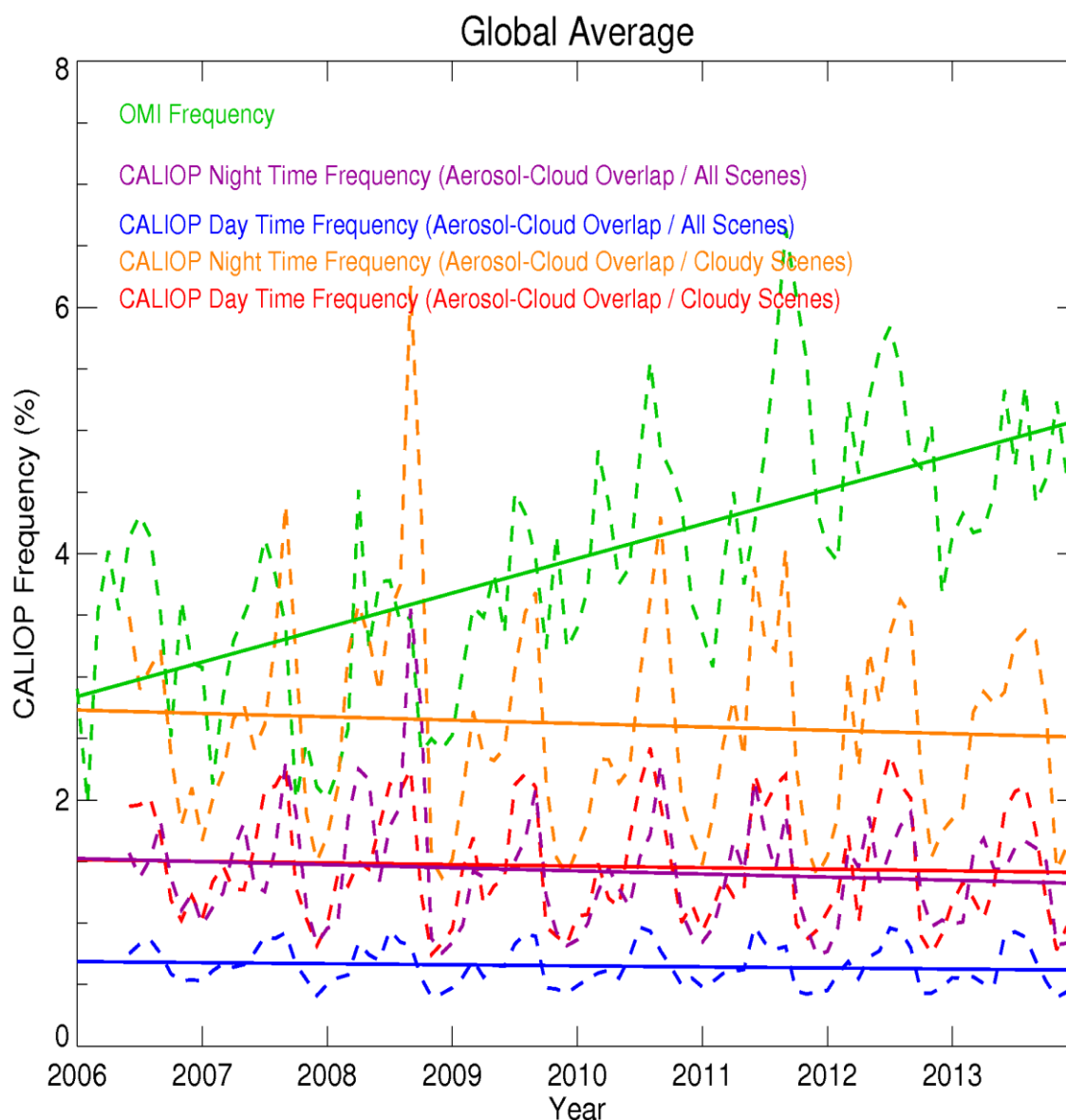


Figure 9. Monthly-averaged global ACA frequencies derived using the OMI-MODIS based method (green) as well as the CALIOP-based method as described in the text. The corresponding baseline thresholds are applied to both CALIOP and OMI data. Dashed lines represent monthly variations in ACA frequencies and the solid lines represent the yearly ACA frequency trends: OMI daytime cloudy-sky frequency is shown in green, CALIOP nighttime cloudy-sky frequency is orange, CALIOP nighttime all-sky frequency is purple, CALIOP daytime cloudy-sky frequency is red and CALIOP daytime all-sky frequency is blue.

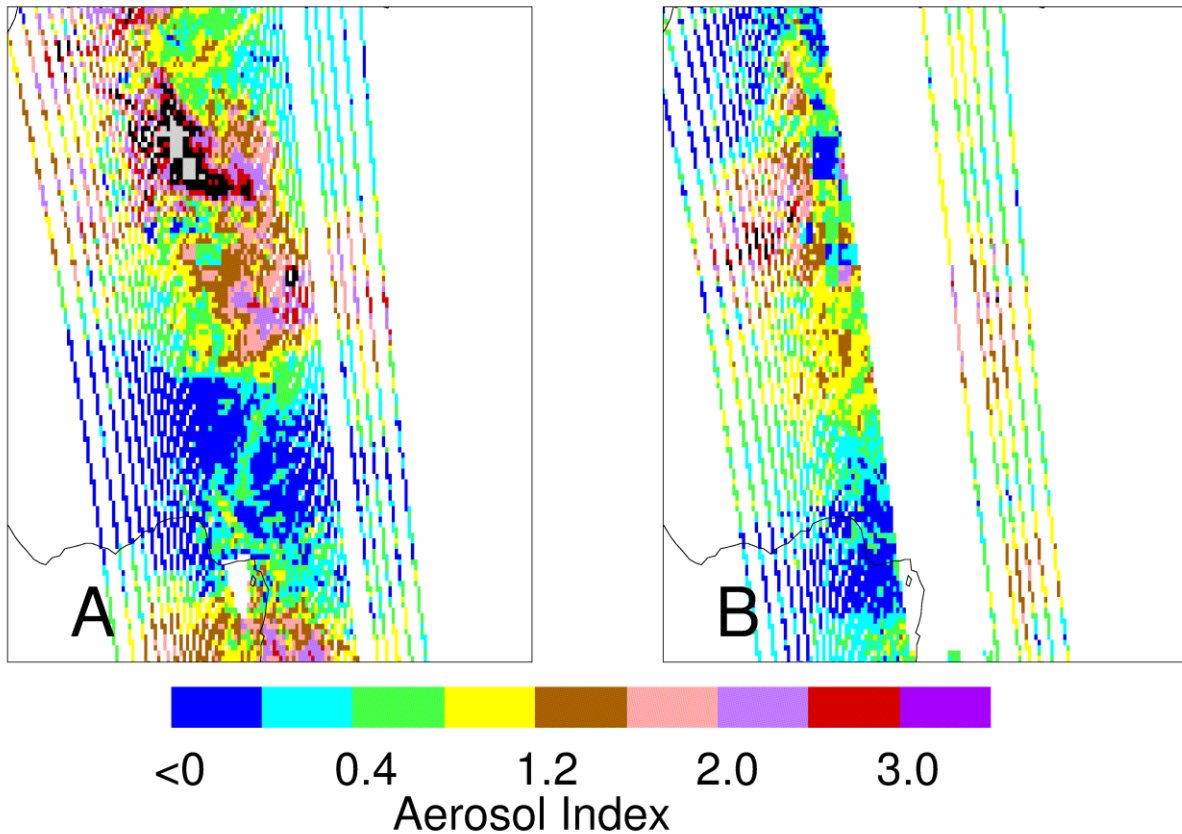


Figure 10. (A) A single swath from the OMI instrument over northern Africa on August 1, 2007 before the significant data loss reported in all OMI aerosol products. (B) A single OMI AI swath over the same region as Fig. 10A on June 1, 2009 which is affected by the significant data loss

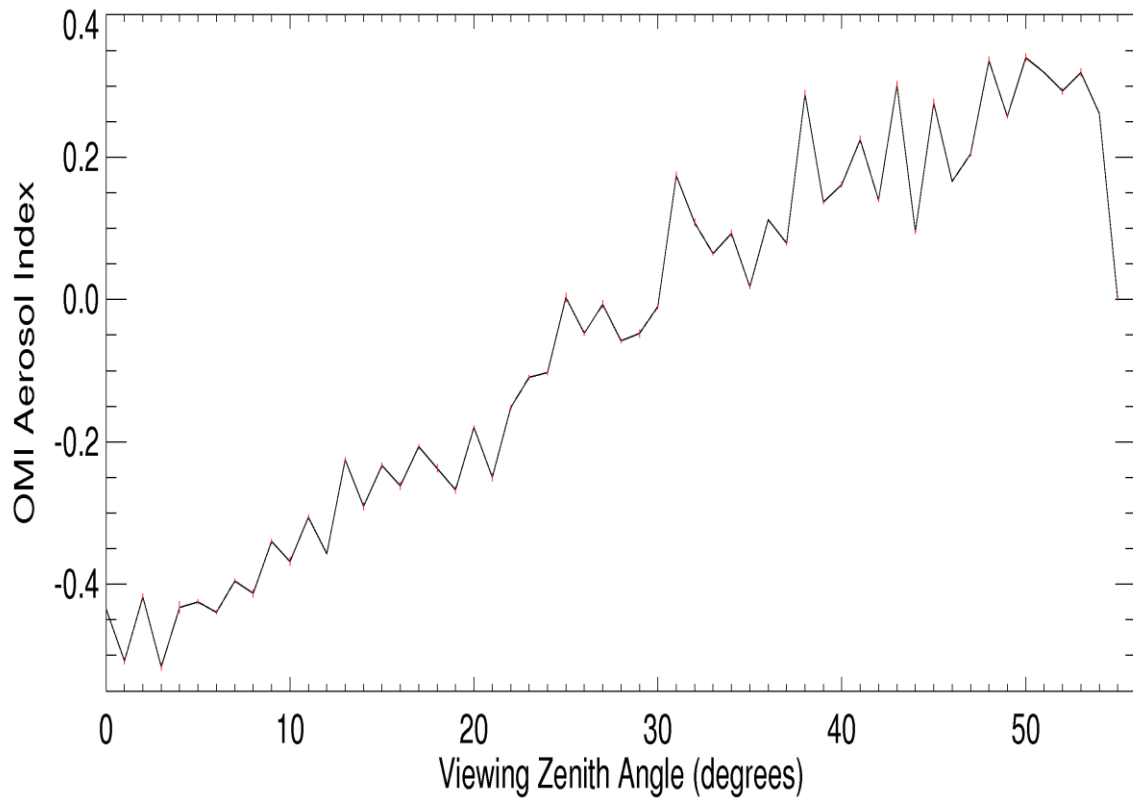


Figure 11. The OMI AI as a function of the sensor's viewing zenith angle (VZA). All OMI AI data over the course of a year (2007) were binned into 1° VZA increments. The red vertical bars represent the 95% confidence interval for each 1° bin.

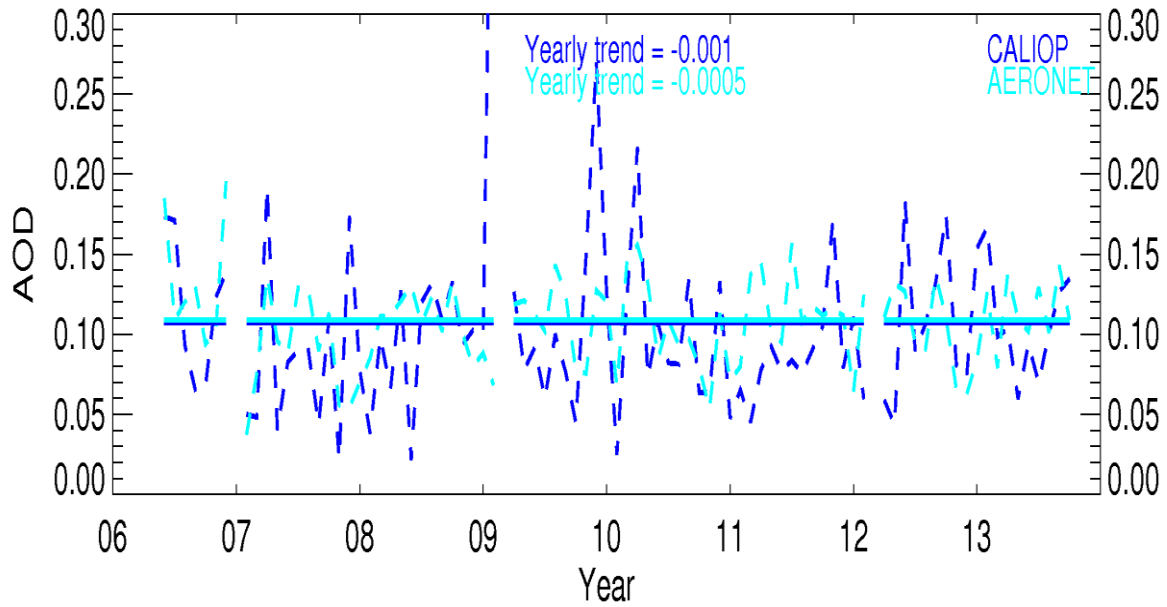


Figure 12. Monthly-averaged over ocean clear-sky AODs derived from collocated CALIOP and AERONET data. CALIOP retrievals within 0.3° latitude and longitude and ± 30 minutes of the corresponding AERONET station and observation are considered collocated. AERONET and CALIOP AODs above 0.2 and 0.6, respectively, are not included in order to avoid high aerosol loading cases and exclude noisy CALIOP data.

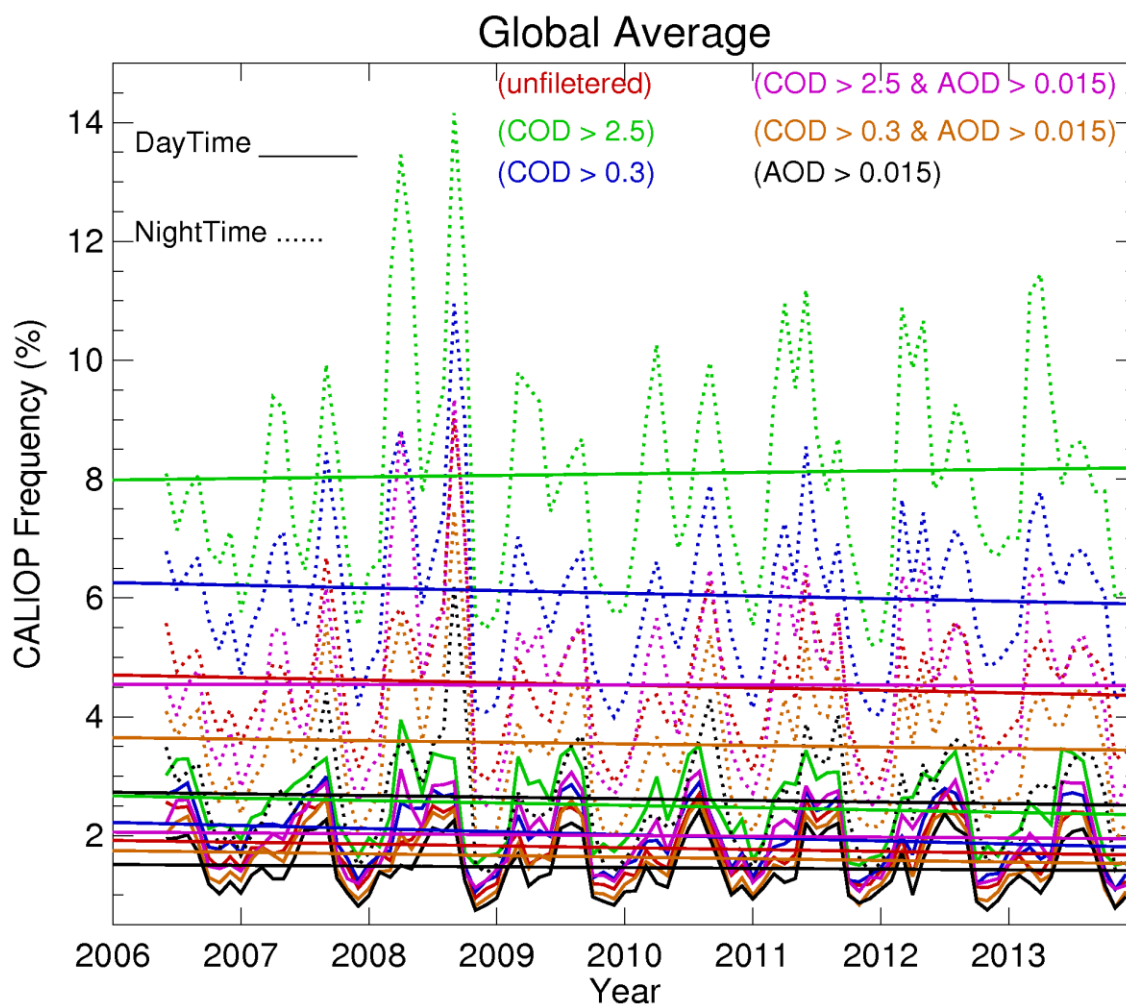


Figure 13. Monthly-averaged global CALIOP cloudy-sky frequencies after applying several different threshold techniques to both day and night time data. The solid lines show the daytime scenario for each respective case while the dotted lines show the nighttime observations for each case.

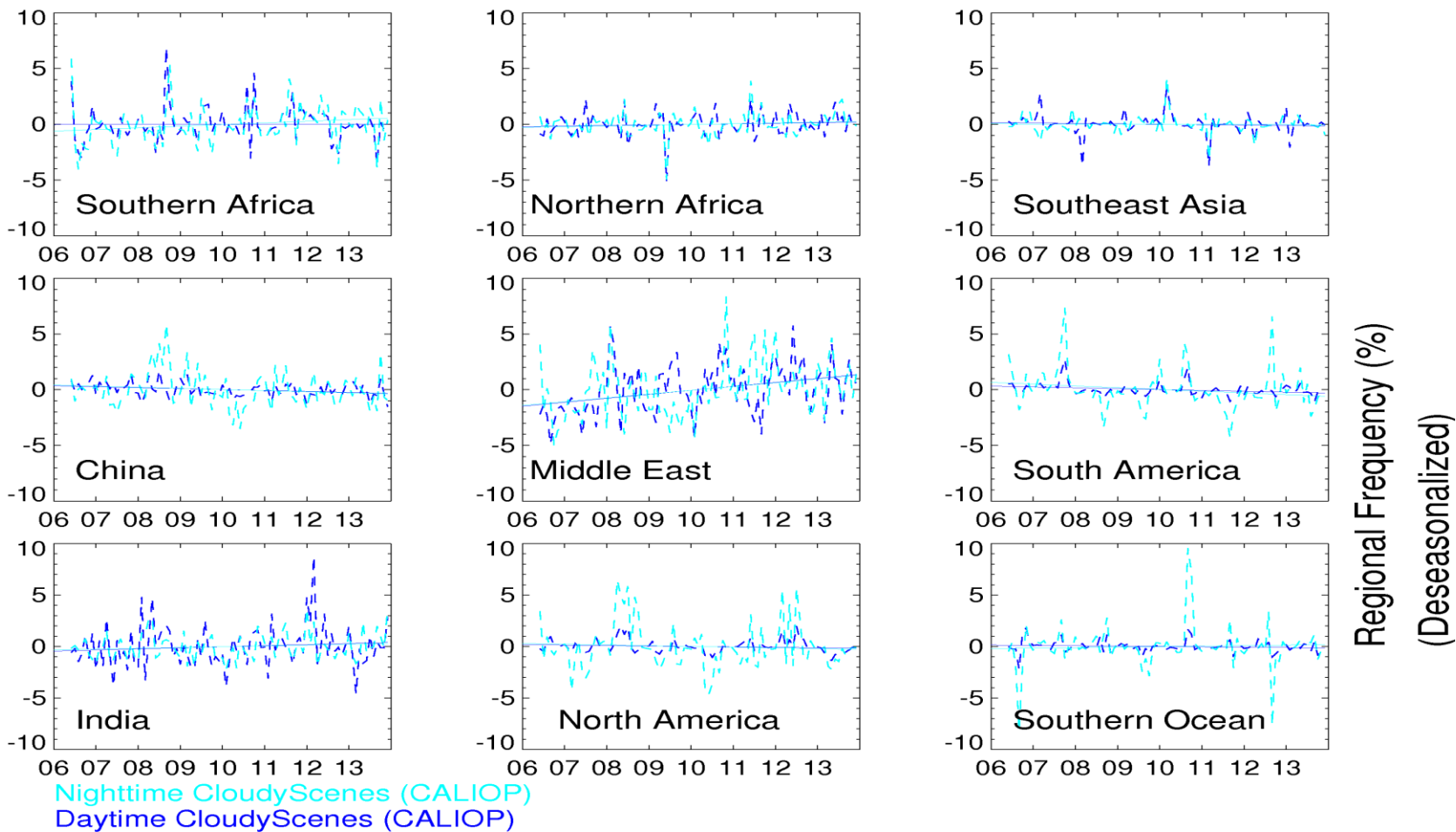


Figure 14. The de-seasonalized monthly- and regionally-averaged cloudy-sky frequency of ACA occurrences for the nine different regions outlined in Fig. 3 and explained in Table 3. The dashed lines show the monthly frequency over the regions and the solid lines show the trend lines computed for each region with the x-axis representing the year of the study. The CALIOP nighttime analysis is shown in aqua marine and the day-time analysis is shown in dark blue.

Table 1. Various definitions of frequency of above-cloud aerosols (ACA) used throughout the study.

Name	Data Set	Definition
Cloudy-Sky ACA Frequency (Passive)	OMI-MODIS	(# of MODIS observation with assigned AI > AI baseline and cloud fraction equal to one) / (# of MODIS observations with cloud fraction equal to one and valid AI retrieval) per latitude and longitude grid over given time period
All-Sky ACA Frequency (Passive)	OMI-MODIS	(# of MODIS observation with assigned AI > AI baseline and cloud fraction equal to one) / (# of MODIS observations with valid AI retrieval) per latitude and longitude grid over given time period
Cloud-Sky ACA Frequency (Active)	CALIOP	(# of CALIOP observations with AOD > AOD baseline located above a cloud with COD > 0) / (# of CALIOP observations with COD > 0) per latitude and longitude grid box over given time period
All-Sky ACA Frequency (Active)	CALIOP	(# of CALIOP observations with AOD > AOD baseline located above a cloud with COD > 0) / (total # of CALIOP observations) per latitude and longitude grid box over given time period

Table 2. Global cloudy-sky relative frequency and data counts for the sensitivity test carried out in Sect. 5. Aerosol and cloud layers retrieved with ‘intermediate’ or ‘strict’ QA metrics are considered in this analysis. A total of five different threshold tests are applied to both day and nighttime CALIOP cloud and aerosol layer products.

	Day	Night
Total Cloudy Scenes (Column COD > 0 /0.3/2.5)	100,028,240/ 54,801,072/ 28,559,920	91,828,232/ 52,634,300/ 25,897,344
Data Counts / Mean Global ACA Relative Frequency		
COD > 0 & AOD > 0	1,193,048/ 1.79 %	3,368,351 / 4.5 %
COD > 0.3 & AOD > 0	789,652/ 2.0 %	2,795,442 / 6.1 %
COD > 2.5 & AOD > 0	556,097/ 2.5 %	2,091,310/ 8.09 %
COD > 0.3 & AOD > 0.015	597,917/ 1.63 %	1,516,547/ 3.54 %
COD > 2.5 & AOD > 0.015	420,778/ 2.0 %	1,167,569/ 4.52 %
COD > 0 & AOD > 0.015	904,892 / 1.46 %	1,765,620 / 2.6 %

Table 3 Seven and a half year above-cloud aerosol cloudy-sky frequency, ACAOD and clear-sky AOD inter-annual variability analysis for the selected target regions. Aerosol and cloud layers retrieved with ‘intermediate’ or ‘strict’ QA metrics are considered in this analysis. Yearly variation for the entire globe is also included. For each region, inter-annual variability (frequency change per year) for the three parameters, the ACA cloudy-sky frequency, ACAOD and clear-sky AOD values are reported. Note that the inter-annual variability for clear sky AODs is estimated using 100% cloud free data from the CALIOP cloud and aerosol layer products.

Region	Latitude (°)	Longitude (°)	Slope /per year (CALIOP day-time) (%)	Trend Significance CALIOP day-time ($\frac{\hat{\omega}}{\sigma_{\hat{\omega}}}$)	Slope /per year (CALIOP night-time) (%)	Trend Significance CALIOP night-time ($\frac{\hat{\omega}}{\sigma_{\hat{\omega}}}$)
ACA cloudy-sky frequency (%) / Above-cloud aerosol AOD / clear-sky AOD						
Southern Africa	37°S - 5°N	30°W - 30°E	0.007/ -0.001/ -0.0004	0.009/ 0.18/ 0.04	0.148/ 0.0005/ 0.0009	0.159/ 0.067/ 0.08
Northern Africa	5°N - 35°N	70°W - 25°E	0.05/ -0.0006/ -0.001	0.116/ 0.035/ 0.07	0.07/ -0.0001/ -0.002	0.133/ 0.005/ 0.09
Southeast Asia	10°N - 25°N	90°E - 150°E	-0.04/ 0.004/ -0.002	0.080/ 0.17/ 0.1	-0.010/ -0.0012/ -0.0004	0.026/ 0.07/ 0.02
China	30°N - 55°N	110°E - 160°E	-0.084/ 0.0006/ 0.0009	0.238/ 0.090/ 0.05	-0.10/ -0.0006/ 0.0002	0.088/ 0.10/ 0.008
Middle East	10°N - 40°N	30°E - 55°E	0.36/ 0.004/ 0.006	0.239/ 0.15/ 0.16	0.339/ 0.004/ 0.005	0.238/ 0.09/ 0.13
South America	20°S - 10°N	105°W - 60°W	-0.078/ 0.0018/ -0.0016	0.189/ 0.18/ 0.12	-0.157/ -0.0002/ -0.0019	0.109/ 0.03/ 0.09
India	0° - 30°N	60°E - 85°E	0.10/ 0.001/ 0.0084	0.106/ 0.08/ 0.20	0.08/ -0.0035/ 0.010	0.110/ 0.064/ 0.19
North America	20°N - 60°N	160°W - 110°W	-0.05/ 0.0005/ 0.00002	0.082/ 0.06/ 0.003	-0.074/ -0.0005/ -0.0003	0.045/ 0.10/ 0.04
Southern Oceans	40°S - 12°S	35°E - 115°E	-0.04/ 0.0004/ 0.0012	0.120/ 0.083/ 0.29	0.05/ 0.0004/ 0.0008	0.037/ 0.078/ 0.21
Global			-0.004/ 0.0004/ 0.0006	0.049/ 0.16/ 0.13	-0.02/ 0.0004/ 0.0007	0.05/ 0.15/ 0.18